

# *Magnetic Domain Imaging of Spintronic Devices*

## 6.1. INTRODUCTION

In the analysis of magnetoelectronic structures, the primary goal of a magnetic imaging technique is to provide a spatially resolved picture of the magnetization vector,  $\mathbf{M}(x,y,z)$ , throughout the sample or device. Knowing this magnetic structure is at the heart of understanding how magnetic devices work. Properties such as the magnetoresistance, the magnetic stray field, and the response to an applied magnetic field all depend critically on the magnetic structure. In this chapter, we will review various methods of imaging magnetic structure. In particular, we will focus on methods that may be applied to spintronic devices and materials.

The magnetization in a magnetic sample can be non-uniform over a large range of length scales for many reasons. For dimensions greater than a micrometer, the most common structures are related to magnetic domains. These are regions where the magnitude of the magnetization is constant, but the magnetization direction varies in order to reduce the stray field emanating from the edges of a magnetized structure. This reduction in energy associated with the long-range magnetostatic interactions is balanced by the cost in the short-range exchange energy of forming domain walls, which typically have dimensions on the order of a tenth of a micrometer. In addition, domain walls may also have internal structure such as chirality and singularities that depend on specific properties of the magnetic system such as film thickness. As the size of the magnetic system becomes smaller, concepts such as domains and domain walls may no longer apply, but the magnetization may still have structure. For example, magnetic particles or lithographically patterned thin film elements that are smaller than a domain wall width might be expected to be single domain, yet these structures quite often exhibit some partial rotation of the magnetization near their edges. Finally, for dimensions less than a nanometer, a continuum picture of uniform magnetization no longer applies and one must consider the magnetization at the atomic scale. For example, different elements in an alloy may have different magnetization, or the atomic moments near an interface may be different than in the bulk.

Although magnetic domain structures can be quite complicated, the fundamental physics governing their formation is well known. The domain structure is determined by minimizing the total energy, which consists primarily of contributions from

the exchange, anisotropy, self-field, applied field, and magnetostriction. In fact one might reasonably ask why we need magnetic imaging techniques at all; why cannot we simply compute the magnetic structure? The answer, for systems larger than a few micrometers lies in the complexity and variety of possible domain structures. In such cases, magnetic domain theory can be used to *explain* the observed domain structures, but theory usually cannot *predict* the domain structure. For smaller, simpler structures, single domain patterned thin film elements, e.g., micromagnetic modeling has become much more successful at predicting magnetic structures.<sup>1</sup> Real magnetic devices, however, are usually more complicated than the simple model structures, so that magnetic imaging tools are still necessary in order to understand why a real magnetic device does not behave in the same way as its model counterpart.

We can ask what sort of information an ideal magnetic imaging technique would provide. It should be able to image the magnetic structure with nearly atomic resolution both laterally and as a function of depth. It should be able to image the magnetization while applying an arbitrary magnetic field. The imaging technique should be fast enough to follow the magnetization dynamics on a timescale comparable to that of the spin precession. To be useful to device manufacturers, the technique should be able to image the magnetization in working devices that may be buried under non-magnetic overlayers or deposited on top of complex structures. Finally, all of this imaging must be done without disturbing the magnetic structure of the device. No single, current imaging technique can satisfy all of these demands, but some are better at particular aspects. In order to get a more complete picture of the magnetic structure, therefore, multiple complementary imaging methods should be used whenever possible.

There are several general comments that apply to every magnetic imaging technique we discuss. First, the contrast is related either to a sample's magnetization or to the magnetic field produced by that magnetization. While the magnetic field can always be calculated from the complete magnetization distribution, determining a unique magnetization distribution from the magnetic field is not possible. However, in the case of magnetic recording media, e.g., the stray field image may be the desired information. Second, probing depths limit all of the methods to, at most, the top few micrometers of a sample. This surface sensitivity is usually not a problem for thin films, but it means that bulk domain structures cannot be directly determined. Third, all of the techniques require smooth, damage-free surfaces. In general, surfaces need to have a mirror finish, so that topography or surface stress does not affect the measurement. Fourth, correlations may exist between parameters describing a technique. For example, it may be impossible to achieve a technique's ultimate magnetic sensitivity at the highest possible resolution. Finally, most of the techniques use digital signal acquisition and rely heavily on modern image processing tools.

In the following sections, we discuss several techniques that are particularly well suited for imaging the magnetic microstructure in the types of structures one might encounter in dealing with spintronic devices. Specifically, we limit our discussion to scanning electron microscopy with polarization analysis (SEMPA), transmission electron microscopy (TEM), magneto-optic, magnetic force microscopy (MFM), and magnetic circular dichroism (MCD). More complete reviews of these and other domain imaging techniques are available.<sup>2,3</sup>

## 6.2. SCANNING ELECTRON MICROSCOPY WITH POLARIZATION ANALYSIS

Scanning electron microscopy with polarization analysis directly provides an image of the surface magnetization of a sample. SEMPA measures the spin polarization of the secondary electrons that exit from a magnetic sample as the finely focused (unpolarized) beam of the scanning electron microscope rasters over the sample, as shown schematically in Fig. 6.1. SEMPA depends on the fact that the polarization of the secondary electrons reflects the net spin density of the material.

For the purposes of SEMPA, it is sufficient to treat each component of the vector polarization separately. The polarization along the  $x$ -direction is

$$P_x = (N_{\uparrow} - N_{\downarrow}) / (N_{\uparrow} + N_{\downarrow}) \quad (6.2.1)$$

where  $N_{\uparrow}$  ( $N_{\downarrow}$ ) are the number of electrons with spins parallel (antiparallel) to the  $x$ -direction. Measurements of the energy distribution of spin polarized electrons from a ferromagnet showed a significant polarization of the secondary electron peak suggesting<sup>4</sup> the possibility of using this effect for magnetic imaging.<sup>5,6</sup> There is even an enhancement of the polarization at low secondary kinetic energy. In a ferromagnetic material, there are more unfilled minority (down spin) states for electrons to scatter into during the secondary cascade process, thereby preferentially filtering out minority spin electrons and increasing the polarization.<sup>7</sup> At higher kinetic energies, between 10 and 20 eV, there is reasonably a good agreement between the measured polarization for Fe, Co,<sup>8</sup> and Ni<sup>9</sup> and the expected polarization, 28, 19, and 5% for Fe, Co, and Ni, respectively. Here, we assume the cascade electrons represent a uniform excitation of the valence band. In this simple model,

$$P = n_B / n_V \quad (6.2.2)$$

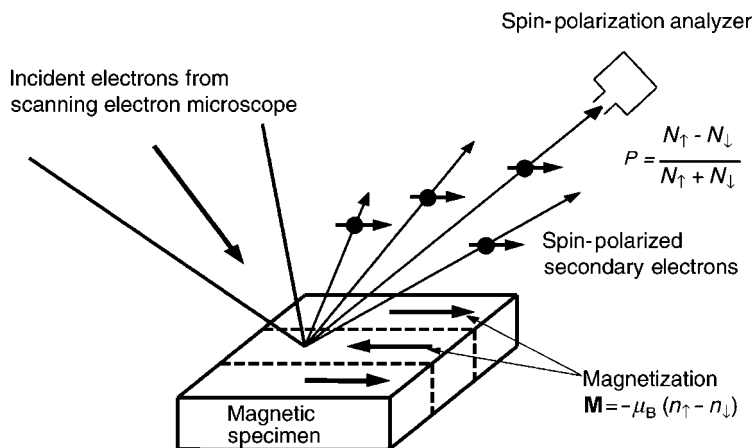


Figure 6.1. A schematic depiction of SEM with SEMPA apparatus. Spin-polarized secondary electrons, emitted when a finely focused incident electron beam hits the sample, are spin analyzed to determine the magnetization direction in the region under the incident beam.

where  $n_v$  is the total number of valence electrons per atom and  $n_B$  is the number of Bohr magnetons per atom. Since the Bohr magneton number is the net spin density per atom ( $n_\uparrow - n_\downarrow$ ), the measured polarization is directly related to the spin part of the magnetization, which is

$$\mathbf{M} = -\mu_B(n_\uparrow - n_\downarrow) \quad (6.2.3)$$

The magnetization and polarization are of opposite sign because the electron spin magnetic moment (units of the Bohr magneton,  $\mu_B$ ) and the electron spin are in opposite directions. The spin part of the magnetization is a close approximation to the total magnetization in a transition metal ferromagnet where the orbital moment is quenched.

In this chapter, our aim is to illustrate the features of SEMPA, both strengths and weaknesses, which should be considered for applications to domain imaging of spintronic devices. Further discussion of the detailed implementation of SEMPA can be found elsewhere.<sup>10-13</sup>

The spatial resolution is determined largely by the electron beam diameter of the SEM. Because the beam current decreases rapidly with decreasing beam diameter, there are practical resolution limits. These restrictions are determined by the current required to obtain a polarization image in a reasonable time (limited by sample drift, deterioration of the sample surface, and operator patience). As a rule of thumb, a beam current of  $\sim 1$  nA is required to obtain a SEMPA image in about 1 h; this leads to resolution limits of approximately 50 nm for LaB<sub>6</sub> and 10 nm for field emission SEM electron gun cathodes. Better spatial resolution is obtained for SEM intensity images that do not suffer from the inefficiency of electron spin polarization analyzers.<sup>10-13</sup>

SEMPA is a surface sensitive technique with a probing depth of about 1 nm because of the short escape depth of secondary electrons. Therefore, sample surfaces must be clean; contaminants would dilute the polarization or, in the case of a thick overlayer, obscure it completely. Conventional surface science preparation techniques are used to prepare SEMPA samples *in situ*. Samples fabricated elsewhere and inserted into the SEM will have a layer of surface contamination, such as a surface oxide, that can be removed by ion bombardment. Depending on the sample, the ion bombardment may be accompanied by annealing, to relieve any induced strain. An ultrahigh vacuum environment is required in the SEM chamber. Commercial scanning electron microscopes with ultrahigh vacuum capability are usually sold as scanning Auger microprobes. Compositional mapping is then also available to correlate with the magnetic images. In certain cases, ion milling and the Auger analysis may be combined with SEMPA to depth profile the magnetic structure of multilayer devices, e.g., a Cu/Co GMR structure.<sup>14</sup> SEMPA enjoys other advantages that are typical of an SEM. These include a large depth of field, easily variable magnification to look at regions of the surface ranging from a few millimeters to a few hundred nanometers, and a large working distance. Image acquisition time runs from 1 to 100 min, depending on resolution, magnetization, and image size. SEMPA has a high sensitivity and can detect a couple of tenths of an atomic layer of Fe, which at high resolution corresponds to about  $10^3$  atoms or  $10^{-17}$  emu. On the negative side, stray magnetic fields ( $\geq 10$  Oe) must be avoided. In addition, to avoid charging effects, conductive samples are required.

An example of a SEMPA magnetization image of the surface of a Fe-3%Si single crystal is shown in Fig. 6.2. The intensity and two components of the magnetization are imaged simultaneously in a SEMPA measurement. The intensity image of Fig. 6.2(a) is the familiar topography image of the SEM. This image is obtained from the sum  $(N_{\uparrow} + N_{\downarrow})$ , which appears in the denominator of Eq. (6.2.1). Spin analyzers are capable of measuring two components of the magnetization which in Fig. 6.2(b) and (c) are the  $x$  and  $y$  components in the plane of the sample. The magnetization is expected to lie in plane to minimize the magnetostatic energy. Out-of-plane magnetization, which is present in special circumstances, can be measured by electrostatically diverting the secondary electrons to a spin analyzer at  $90^{\circ}$  with respect to the one that measures the in-plane components<sup>15</sup> or by using a spin rotator.<sup>16</sup> In the  $M_x$  image, white corresponds to magnetization to the right and black to the left. The intermediate gray regions correspond to magnetization in the  $y$ -direction which are seen as white and black in the  $M_y$  image for up and down magnetization, respectively. The magnetization is expected to be uniform in magnitude which can be tested by processing the signal to obtain the magnitude,  $(M_x^2 + M_y^2)^{1/2}$ , shown in Fig. 6.2(d). The reduced magnetization at the domain walls is an artifact and does not represent an out of plane  $M_z$  component of a Bloch wall. Close inspection at high resolution reveals that the walls at the surface are in-plane Néel caps on the interior Bloch walls. The domain wall artifacts in image Fig. 6.2(d) occur for a lower-resolution image such as this when the beam is wider than the wall.

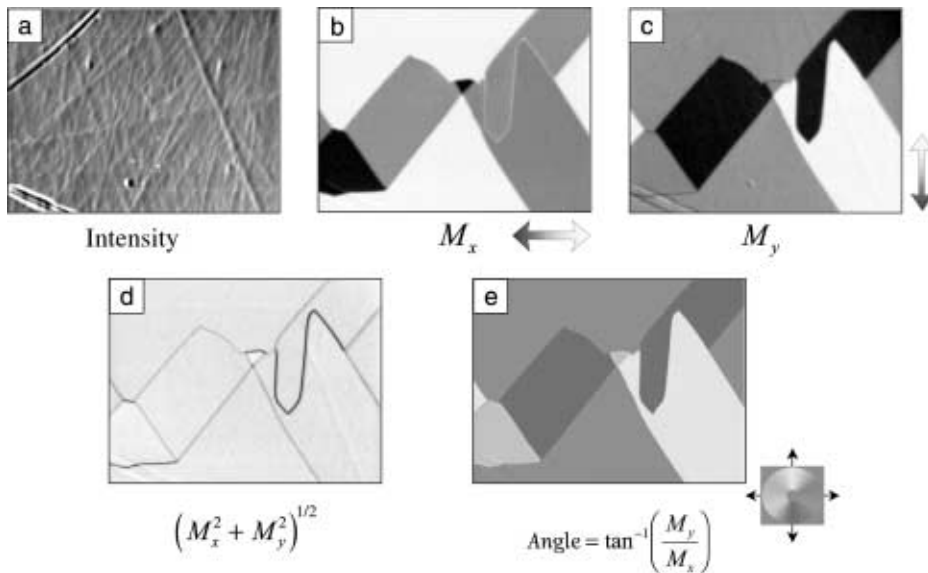


Figure 6.2. SEMPA images of an Fe-3%Si single crystal. (a) An intensity image showing the topography as would normally be seen with an SEM. (b) Polarization image where the gray scale intensity is proportional to the component of the magnetization in the  $x$ -direction. (c) Polarization image for  $y$  component of magnetization. (d) Image of the magnitude of the observed polarization computed from the measured  $M_x$  and  $M_y$  components. (e) Image giving the direction of the magnetization as computed from the measured  $M_x$  and  $M_y$  components.

Then, electrons excited from each side of the wall add to a zero polarization for a  $180^\circ$  wall and a reduced polarization for a  $90^\circ$  wall. In Fig. 6.2(e), the angle of magnetization, which equals  $\tan^{-1}(M_x/M_y)$ , is calculated and plotted in color with the directions corresponding to the accompanying color wheel.

The images of Fig. 6.2 illustrate some characteristics of SEMPA. First, the magnetization vector  $\mathbf{M}$  is imaged, not the stray magnetic field  $\mathbf{H}$ . Any two components of  $\mathbf{M}$  can be simultaneously imaged with the topography. The images are formed with the same electrons from exactly the same sample area so features present in the magnetic microstructure can be directly correlated with the surface topography. The magnetization image should be independent of the topography as can be seen from Eq. (6.2.1). Nevertheless, sometimes “topographic feedthrough” can be seen as is evident from scrutiny of the lower left region of Fig. 6.2(a) and (c). A procedure involving a second measurement exists to minimize the topographic feedthrough further.<sup>13</sup> Topographic feedthrough is a particular problem at edges, such as would be encountered in a thin film magnetic element, and special care is necessary to measure such structures at high resolution.

As an illustration of the SEMPA technique, we show some results of SEMPA applied to the study of the coupling of ferromagnetic layers separated by non-magnetic layers. Artificially layered magnetic structures allow one to tailor transport and magnetic properties to fit special requirements, such as for giant magnetoresistance or spin valve devices. As a first example in Fig. 6.3, we show three stages of creating an Fe/Cr/Fe(001) trilayer. The top panels, a–c, display  $M_y$ , and the bottom panels, d–f, display  $M_x$ . Figure 6.3(a) and (d) at the left shows magnetization

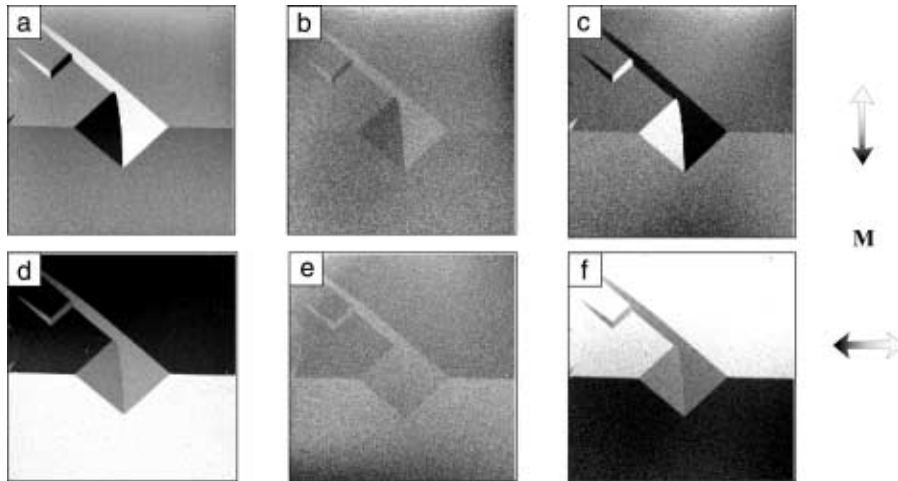


Figure 6.3. SEMPA images displaying the magnetization observed in different layers of an Fe/Cr/Fe trilayer. (a) Shows the  $M_y$  component of the magnetization of an interesting domain structure on an Fe whisker substrate. (b) Shows the same region after deposition of 1 nm of Cr. (c) Shows the same region following the addition of 2 nm of Fe to make a Fe/Cr/Fe trilayer. Note the reversal of magnetization directions between (a) and (c). (d–f) The  $M_x$  component of magnetization for the same conditions as in (a–c).

images of the clean Fe(001) single crystal whisker. There is a domain wall running horizontally, with  $M_x$  in the bottom of the whisker to the right and the top half to the left. There is a diamond-shaped domain in the middle with magnetization exhibited in the  $M_y$  image. The middle panels show this same region of the whisker after deposition of 1 nm of Cr. The domains of the whisker are largely obscured but can still be discerned through the 1 nm of Cr, giving a vivid visual demonstration of the probing depth of SEMPA. The images at the right show the magnetization at the surface of a 2 nm Fe layer deposited on top of the Cr. Note that each component of the magnetization in this trilayer sandwich is antiparallel to that on the clean Fe whisker. This antiparallel coupling of two Fe layers separated by a particular thickness of Cr was first observed by Grünberg *et al.*<sup>17</sup> Parkin *et al.*<sup>18</sup> subsequently found that the coupling of the layers oscillated between antiferromagnetic and ferromagnetic depending on the thickness of the spacer layer.

In order to study the dependence of the interlayer coupling on the thickness of the spacer layer, SEMPA was applied to measure the magnetization of the top layer of a structure like that shown in Fig. 6.4(a).<sup>19</sup> In this structure, the thickness of the Cr spacer is varied continuously in a very shallow wedge that increases approximately 10 nm in thickness over approximately 1 mm in length. In contrast to the alternative method of creating trilayer structures as in Fig. 6.3, where fluctuations in preparation conditions could occur from one film to the next, the wedge structure provides all spacer layer thicknesses in a single deposition. In the case of layer by layer growth of the Cr, it is possible to use the SEM, equipped with a phosphor screen below the sample, to do reflection high energy electron diffraction (RHEED) along the wedge. In this way, one can obtain a very accurate measure of the wedge thickness from the RHEED intensity oscillations.<sup>19</sup>

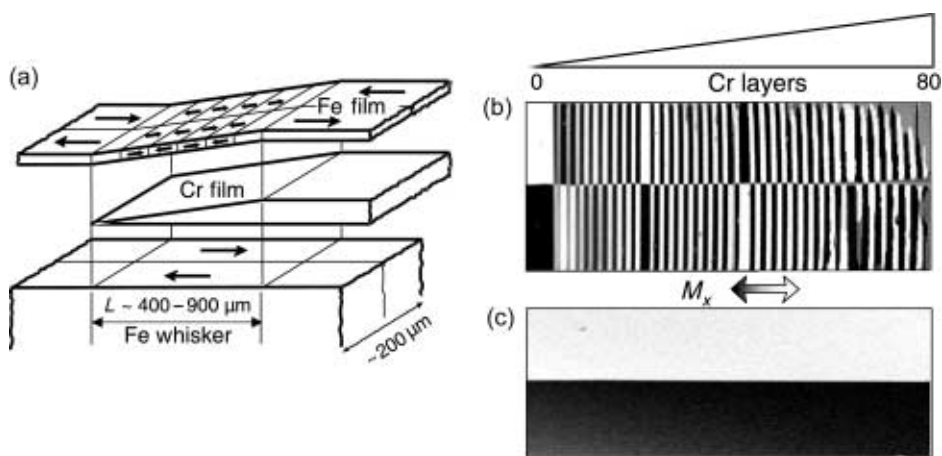


Figure 6.4. (a) A schematic depiction of the Fe/Cr/Fe wedge geometry, as used in SEMPA. It consists of a single crystal, Fe whisker substrate with two oppositely directed domains, an epitaxial Cr layer with a linearly varying average thickness, and an epitaxial Fe overlayer. (b) The  $M_x$  component showing the alternation of magnetization direction of the Fe overlayer with each single layer increase in the Cr layer thickness. (c) A SEMPA measurement of the magnetization of the bare Fe substrate. Modified from Ref. 19.

Magnetization images from this wedge structure are shown in Fig. 6.4(b) and (c). The  $M_x$  image of the clean Fe whisker with two domains is shown in Fig. 6.4(c). The magnetization of a 2 nm Fe layer grown on top of the Cr wedge is shown in Fig. 6.4(b). The Cr was grown at an Fe substrate temperature of approximately 300°C which produces layer by layer growth. The magnetization of the Fe overlayer is coupled ferromagnetically to the whisker up to a thickness of four Cr layers and then reverses the direction of the coupling with each additional Cr layer thickness. This reversal continues until at a thickness of 24 layers, the Cr thickness increases by two layers before the Fe magnetization reverses. This phase slip in the reversal process that occurs again at 44 and 64 layers results because the period of the oscillatory exchange coupling is measured to be  $2.105 \pm 0.005$  layers, which is slightly incommensurate with the lattice spacing. Such a precise determination of the period by SEMPA was possible because of the many oscillations observed and the accurate thickness measurement from RHEED intensity oscillations. SEMPA, which is uniquely suited for such studies, provided precise measurements of the periods of oscillatory coupling which could be tied to Fermi surface properties of the spacer layer. On the other hand, to measure the strength of the coupling requires the application of magnetic field that would disturb the secondary electrons. For coupling strength measurements, samples prepared and checked in the SEMPA system had to be coated with an Au protective layer for measurement in a Kerr microscope<sup>20</sup> as described in Section 6.4.

As a final example of SEMPA applications, we show a magnetization image of an array of Fe nanowires in Fig. 6.5. The array was fabricated by oblique deposition of Fe onto a template of Cr lines made by laser-focused atom deposition.<sup>21</sup> The Fe wires are approximately 100 nm wide and 0.15 mm long, spaced by 213 nm. The low magnification image of Fig. 6.5(a) shows the Fe nanowires as white lines with magnetization  $M_y$  up, and black lines with magnetization down. The gray regions between the white and black domains correspond to the nonmagnetic Cr underlayer exposed between the magnetic Fe lines. Where there is a magnetization reversal (change from white to black in the image), there must be a domain wall.

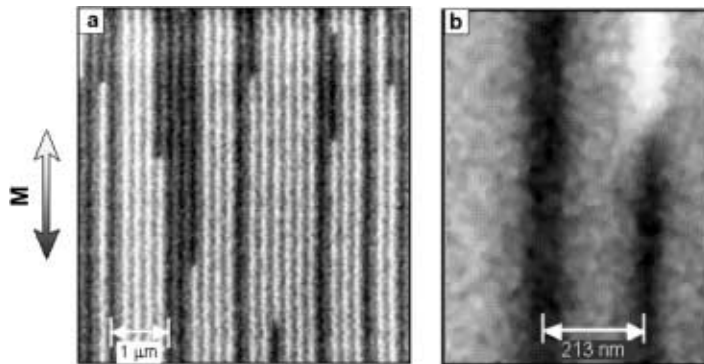


Figure 6.5. (a) SEMPA image of an array of Fe nanowires showing their in-plane magnetization,  $M_y$ , where white (black) indicates up (down). (b) A high-resolution SEMPA image showing a domain wall within a wire. From Ref. 21.

A high-resolution image of such a region is shown in Fig. 6.5(b). It can be seen that the domain wall forms at an angle of  $45^\circ$  with respect to the Fe lines.

In summary, SEMPA has a number of features useful for measurements on spintronics devices. It provides images of two components of the magnetization that are independent of the topography, which is imaged simultaneously. It is a non-perturbative measurement that offers high spatial resolution. At the same time, SEMPA maintains the depth of field capability of an SEM and the ability to look at large areas and then magnify regions of interest. It is a surface sensitive technique, which can be advantageous for investigating thin film devices.

### 6.3. MAGNETIC FORCE MICROSCOPY

Magnetic force microscopy<sup>22–24</sup> developed as an extension to atomic force microscopy (AFM),<sup>25</sup> is the most widely used technique for domain imaging on the nanometer scale. In AFM, a sharp tip, i.e., 10–20 nm in radius, is scanned along the surface of the sample in a non-destructive manner. This is accomplished by mounting the sharp probe at the end of a highly compliant cantilever and sensing the interaction between tip and surface in a variety of ways. In the contact mode, the deflection of the very soft cantilever is detected and used to generate a topograph. In the non-contacting mode, the attraction of the long-range van der Waals force is sensed through its effect on the natural resonant frequency of the cantilever. Finally, in the intermittent contact mode the tip probes the repulsive part of the van der Waals potential, i.e., taps the surface, once for each oscillation.

Magnetic sensitivity is obtained by coating the silicon tip of the cantilever with a ferromagnetic coating to add a magnetic interaction between the tip and the surface. Although a smooth surface is needed, it is possible to sense the magnetic field through non-magnetic layers so surface cleanliness is not of great importance. This allows for in-air imaging and greatly simplifies imaging structures that, in practice, use coatings. Resolutions in the range of 40–90 nm have been demonstrated<sup>26</sup> and non-conductive samples can be used. It is also convenient to be able to apply an external magnetic field of up to about 800 kA/m in strength. As a relatively inexpensive add-on to commercial AFMs, this technique has found a wide audience, particularly within the magnetic information storage industry.

While it is invitingly simple to view this as the interaction of a “magnetic monopole” tip experiencing a force dependent on the magnetic field above an unperturbed ferromagnetic sample, the real situation is far more complex. In actuality, the tip and the sample each consist of a distribution of both surface and bulk magnetic charges that may interact with each other. Interpreting an MFM image means understanding the relationship between the two distributions of magnetic multipoles, the exact nature of which may vary to minimize the total magnetostatic energy of the system.

In domain imaging, the objective is generally to visualize the magnetization of a sample. In the ideal case, an MFM measurement would produce an image related to the stray field above the sample and from this measured field distribution the sample magnetization would be deduced. Unfortunately, it is not possible to uniquely determine the sample magnetization from the field distribution. Further, the imaging mechanism for the MFM is complex and the instrument response is

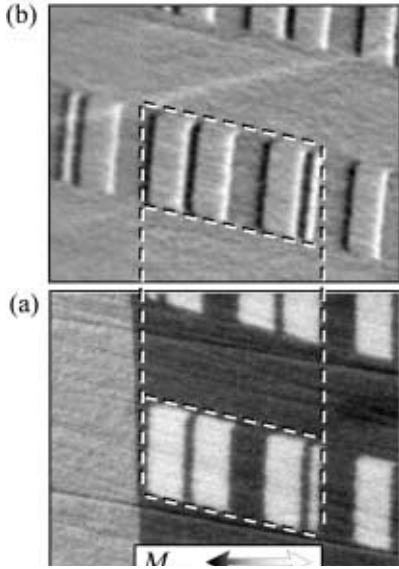


Figure 6.6. (a) A SEMPA image showing the  $M_x$  component of the magnetization of a high density bit pattern written on a hard magnetic disk. (b) Same structure shown in (a) as imaged using MFM. An Au mask, which can be seen in (a), covers the left-hand side of the sample. From Ref. 27.

difficult to quantify. Generally, the MFM does not respond to the magnetic field, but is usually much more sensitive to the higher spatial derivatives of the field components. This means the MFM generally produces images that denote the positions of magnetic charge, e.g., the magnetic charge present inside of domain walls. Such a charge can be thought to arise from the divergence of the magnetization, i.e.,  $-\nabla \cdot \mathbf{M}$ , internally and at surfaces.

In order to discuss how magnetization information might be inferred from MFM data, and better understand the MFM imaging process, we will compare measurements of the same domain structure as seen by SEMPA and MFM. In Fig. 6.6(a), we see a SEMPA<sup>27</sup> image of the magnetization of a magnetic bit pattern written on a thin film recording disk<sup>28</sup> and in Fig. 6.6(b) an MFM image<sup>27</sup> of exactly the same region. Note how the Au mask reduces the magnetization measured by SEMPA to zero while the long range of the magnetic field allows the MFM to still image the region through the Au.

Ideally, given the magnetization determined by the SEMPA measurement, it should be possible to predict the MFM response. The line traces shown in Fig. 6.7 were calculated based on the bit pattern seen in the SEMPA results of Fig. 6.6(a). The top trace reflects the  $x$  component of the magnetization,  $M_x$ , as seen in SEMPA. White (black) areas are magnetized to the right (left). The next lower trace depicts the  $x$  component of the field,  $B_x$ , as calculated from  $M_x$ , at a distance of 100 nm above the sample surface. Next, we calculate and plot  $B_z$ , the  $z$  component perpendicular to the surface, and the first and second spatial derivatives of  $B_z$ . Assume the tip to be a monopole, i.e., it is long, slender, and magnetized along its length (in the  $z$ -direction) so opposite poles are located either near the surface or far from the sample's fields. The interaction between tip and  $B_x$  would then produce a force in the  $x$ -direction that would not be sensed by the MFM, and an interaction with  $B_z$  that would. Note from the  $B_z$  trace that the domain walls appear as either maxima or

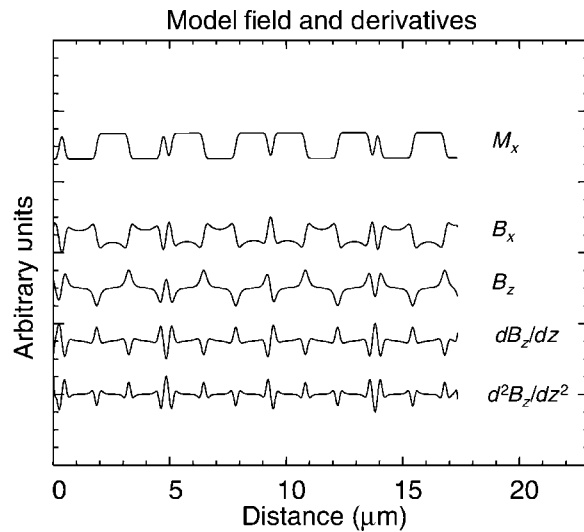


Figure 6.7. A magnetization distribution modeled after the SEMPA measurements shown in Fig. 6.6(a) and several fields and field gradients derived from that distribution. From Ref. 27.

minima while within the domains the value of  $B_z$  is roughly the same independent of the sign of  $M_x$ . This argument would predict that MFM domain images of recorded bits would tend to have alternating bright and dark domain boundaries with the bits themselves appearing gray, independent of their magnetization direction, exactly the appearance seen in Fig. 6.6(b). Notice how the alternating light and dark domain edges give the illusion of height to some bits and appears to distinguish between those magnetized to the right and to the left. A line trace through the MFM image of these bits shows little or no difference in intensity between domains magnetized to the right or left.

An alternative imaging model involves sensing the force gradient, either by measuring the effect of the field gradient on a monopole tip oscillating above the surface or the force on a static dipole tip. Either of these cases corresponds to the derivative curve in Fig. 6.7; were a dipole tip to be used in the oscillating mode, the second derivative curve of Fig. 6.7 would best reflect the interaction. With the exception of the  $B_x$  curve, it can be seen that all of the other curves are similar. None display domain contrast; all have structure at domain walls, i.e., at the location of magnetic charge.

Understanding MFM imaging in terms of magnetic charge contrast<sup>29</sup> is dependent on the tip-sample interaction being sufficiently weak as to preclude changes in the magnetic structure of either. Ideal tips would be both hard, e.g., unchanging in their magnetic structure in the sample's field, and simultaneously magnetically weak, e.g., producing a field adequate enough to allow a measurable interaction yet too small to affect the magnetization distribution in the sample. Changes in the magnetic state of the sample or tip that occur for overly strong interactions may be either reversible or hysteretic. The latter are demonstrated when MFM tips are used to set the state of a magnetic bit,<sup>30</sup> for example. Such changes

may limit the applicability of MFM imaging in the study of low coercivity thin films used in spintronic devices.

Changes in height during scanning introduce another complication in MFM image interpretation. In trying to predict the MFM instrument response to the fields calculated in Fig. 6.7, it is important to remember that each trace is calculated for a fixed tip-sample distance. The MFM may vary this distance during each scan to maintain a constant force. More significant is the fact that surface topography variations will feed through and appear in the MFM magnetic image. Techniques have been developed to minimize this effect.<sup>31,\*</sup> The most popular method, called the interleave or “liftmode,”<sup>\*</sup> makes two scans. First, a scan of the surface is made in the intermittent contact mode to determine the topography. Second, a scan is made in which magnetic forces are sensed while the tip is programmed to follow a constant height contour determined from the topography. In this way, separate topographic and magnetic images can be obtained. Of course, tapping the surface with a magnetic tip in the initial scan may significantly modify the magnetic structure of the sample or the tip.

The MFM offers several important advantages when applied to spintronic devices. It is readily available as a commercial instrument that will provide high-resolution images of domain wall locations with resolution in the tens of nanometers range. External magnetic fields can be applied to observe device response and the MFM can image through non-magnetic overlayers. The sample need not be thinned, so spintronic devices on thick substrates present no difficulty.

Sample topography can present a problem that needs to be considered. Imaging is over a limited area and is slower than most of the other methods so it may be necessary to use MFM in conjunction with a different survey method or have other means of locating the area of study. Image formation is complex and images may be difficult to interpret in terms of a unique distribution of the underlying magnetization. This will present a particular problem in small spintronic devices where there are no domain walls, but it is the subtle changes in magnetization direction that are important to image and understand. Perhaps most difficult is obtaining a probe that will neither modify the magnetic configuration of the device under study<sup>32</sup> nor change its own magnetic configuration.

#### 6.4. MAGNETO-OPTIC IMAGING

The weak interaction between polarized light and a material’s magnetization leads to a large variety of very useful domain imaging methods. The primary magneto-optic interactions depend directly on the magnetization, so that most magneto-optic techniques directly image the magnetic structure, or at least the part of the magnetization that is optically active. For optically transparent samples and transmitted light, the magneto-optic interaction is usually referred to as the Faraday

---

\*Digital Instruments, Santa Barbara, California. Certain commercial equipment, instruments, or materials are identified in this paper in order to specify the experimental procedure adequately. Such an identification is not intended to imply recommendation or endorsement by the National Institute of Standards and Technology, nor is it intended to imply that the materials or equipment identified are necessarily the best available for the purpose.

effect, while for reflected light the interaction is commonly called the Kerr effect. The basic magneto-optic interactions, however, are the same for reflected and transmitted lights. Several excellent comprehensive reviews of magneto-optical domain imaging are available.<sup>3,33</sup>

The physics of the complete magneto-optic interaction is well understood, but somewhat complex.<sup>2,34</sup> The primary magneto-optic interactions involve the frequency-dependent interaction of the electric field vector of the polarized light and the dielectric permittivity tensor of the magnetic material. For the purposes of this discussion, however, it is sufficient to treat the magneto-optic interaction simply as a rotation of the polarization plane of linearly polarized light upon reflection from, or transmission through, a magnetic material. Note, however, that this rotation may also be accompanied by a change in phase leading to elliptical polarization of the light.

The relative geometry between the magnetization,  $\mathbf{M}$ , and the polarization,  $\mathbf{E}$ , vectors determines which component of the magnetization will be visible in a particular magneto-optic image. These geometric sensitivities can be determined using a classical Lorentz force picture of the magneto-optic interaction. Polarized light causes electrons in the sample to oscillate with velocity along  $\mathbf{E}$ . The sample magnetization interacts through the Lorentz force with the electrons generating a small polarization component in the direction of  $-\mathbf{M} \times \mathbf{E}$ . However, one must be cautious applying this classical picture. Although it is useful in determining the direction of the magneto-optic signal, the interaction is not due to a classical Lorentz force but to a relativistic spin-orbit interaction with the solid.

Figure 6.8(a) and (b) shows geometries for observing magnetization perpendicular to and in the sample surface plane, respectively. The polar Faraday or Kerr effects are used to image perpendicular magnetization. From Fig. 6.8(a) and applying the simple Lorentz force picture, one can immediately see that the contrast for perpendicular magnetization is maximized for normally incident,  $\theta = 0$ , light and is roughly independent of the incident polarization direction. For in-plane magnetization, several scattering geometries are possible. Figure 6.8(b) shows the most common arrangement known as the longitudinal effect in which the magnetization lies in the scattering plane of the light. The longitudinal effect vanishes for normal incidence light and is a maximum for  $\theta \sim 60^\circ$ . The longitudinal effect can also be observed for polarization perpendicular to the optical scattering plane. The trans-

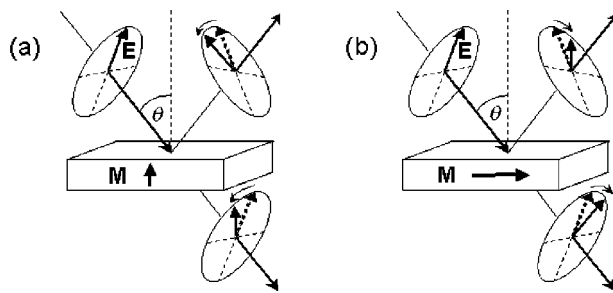


Figure 6.8. Light and magnetization geometries for observing the polar (a), and longitudinal (b) magneto-optic effects for either reflected or transmitted light. Modified from Ref. 2.

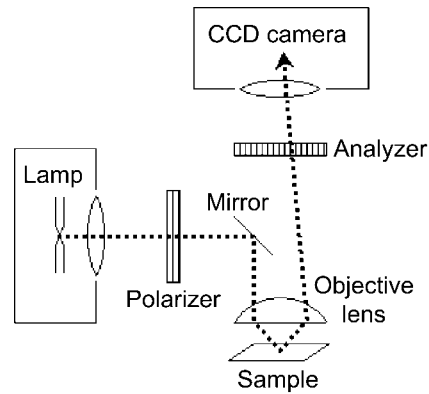


Figure 6.9. A schematic of a magneto-optical microscope for high-resolution imaging of magnetic microstructure in the longitudinal Kerr mode. Modified from Ref. 2.

verse effect allows the observation of magnetization, i.e., in the sample plane, but perpendicular to the scattering plane. The transverse mode is used much less, however, since it does not induce a change in polarization, but only a change in intensity for reflected light and no magneto-optic effect for transmitted light.

Domain imaging instrumentation based on the magneto-optic effects is conceptually straightforward. One simply needs to shine polarized light on a sample and look at the reflected or transmitted light through a crossed polarizer. In practice, however, high-quality optics and significant image processing are required to separate the small magneto-optic signal from the large non-magnetic background.<sup>35–37</sup> A schematic of a high resolution magneto-optic microscope for imaging in-plane magnetization with the longitudinal Kerr effect is shown in Fig. 6.9. These microscopes are usually based on high quality polarized light microscopes that have been specifically modified for magneto-optic imaging. In this case of longitudinal Kerr imaging, the incident and reflected light both pass through the objective lens, and the required oblique illumination and separation of incident and reflected lights is obtained by suitable placement of mirrors and apertures. One interesting feature of this design is that the magnetic contrast increases as the resolution increases, since the numerical aperture increases with increasing magnification resulting in illumination that is more oblique. Typical resolution with this type of microscope is about 1  $\mu\text{m}$ , but using a high numerical aperture oil immersion objective lens and blue light illumination such a microscope can achieve a diffraction limited resolution of 0.3  $\mu\text{m}$ .

Other variations of the basic magneto-optic microscope are possible, each with its own specific advantages.<sup>33</sup> For example, scanned images can also be generated by using a focused laser beam for illumination and rastering either the laser beam or the specimen.<sup>38</sup> The scanned images take longer to acquire than conventional microscopy, but the laser provides very intense illumination and hence a large signal. For larger fields of view and lower magnifications, the illumination and imaging optics for longitudinal imaging are usually separated; however, this leads to imaging a tilted sample and the associated depth of field problems.

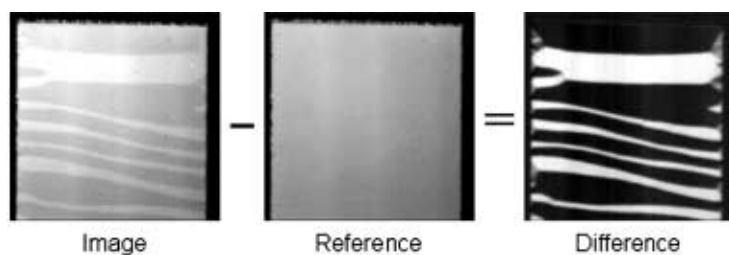


Figure 6.10. An example of digital image subtraction to reduce the non-magnetic background signal in a longitudinal Kerr image. A reference image of the Permalloy rectangle, acquired in a magnetic field large enough to saturate the magnetization, was subtracted from an image acquired at zero applied field.

The small size of the magneto-optic signal, especially in the case of the longitudinal Kerr effect, means that some sort of signal processing is usually required to extract a satisfactory magnetic image. The most common method is to remove the large non-magnetic background signal by taking the difference between the current image and a stored reference image usually taken in a field large enough to saturate the magnetization. In practical terms, this means that magneto-optic imaging is best applied to samples where the magnetization can be changed by applying a field. For static magnetic domain patterns that one cannot or does not want to alter, such as written bits in recording media, high quality, magneto-optic images are difficult to acquire.

Image subtraction is most easily done digitally, so that digital image acquisition with large dynamic range (at least 12 bits) is essential. An example of this method is shown in Fig. 6.10. In this case, the image acquisition and processing with a digital CCD camera and standard software took about 10 s. Near video rate processing is also possible by using a video rate CCD and dedicated image processing electronics.<sup>35,36</sup>

Perhaps the greatest advantage of magneto-optic imaging is the speed with which magnetic images can be acquired. Magneto-optic imaging can yield a great deal of information about magnetization dynamics in a magnetic material or device, since arbitrarily large magnetic fields may be applied to the sample while imaging. While video rate imaging of domain dynamics is routinely achieved using standard arc lamp illumination, pulsed laser illumination can reveal domain wall motion that occurs over timescales as short as a few nanoseconds. Transient changes can occasionally be captured in a single pulse, while reproducible domain motion can be imaged stroboscopically.<sup>39</sup> Some of the best examples of high-speed magneto-optic imaging can be found in studies of domain dynamics in thin film recording heads.<sup>40,41</sup>

The information depth in the Kerr imaging mode is determined by the penetration depth of the light and is about 20 nm in a metal. The technique is, therefore, moderately surface sensitive and can be used to image magnetic domains that are only a few monolayers thick, as well as domains that are coated with thin non-magnetic coatings. Figure 6.11 compares the probing depth of Kerr with that of SEMPA with domain images of a multilayer structure similar to the one described in Fig. 6.4.<sup>20</sup> While SEMPA only sees the magnetization of the top Fe film, the Kerr image contains magnetic contrast from both the top Fe film and the Fe whisker

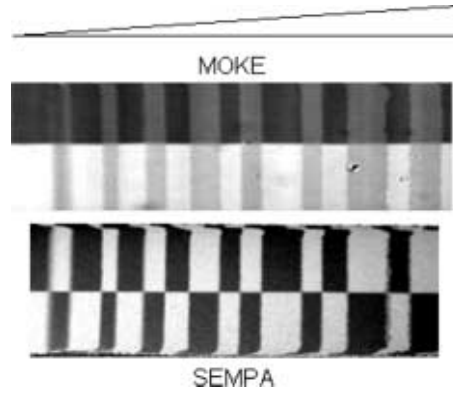


Figure 6.11. Magneto-optic and SEMPA images of the same multilayer structure. The difference in the appearance between the two images is due to the different probing depths of the two methods. The sample consists of an Fe whisker substrate, 0–23 layer Au wedge, 12 layers of Fe, and six Au layer overcoat. Modified from Ref. 20.

substrate. Hence, the reduced contrast for Au spacer layer thicknesses where the Fe film magnetization is opposite to that of the Fe whisker.

The magneto-optic signal can also provide additional information about the layer-dependent magnetization in a magnetic multilayer, because the phase of the reflected Kerr amplitude depends on the depth and the interfaces.<sup>42</sup> This difference in phase can be exploited to selectively cancel the magnetic contrast from a particular layer of the sample, and obtain depth-dependent magnetization information. Figure 6.12 shows an example of this layer-dependent cancellation in an Fe/Cr/Fe wedge multilayer similar to the one described in Fig. 6.4. As the analyzing polarizer angle is rotated, the images either show magnetic contrast from both the top Fe film and the Fe whisker substrate, or from just the Fe film or Fe substrate alone.

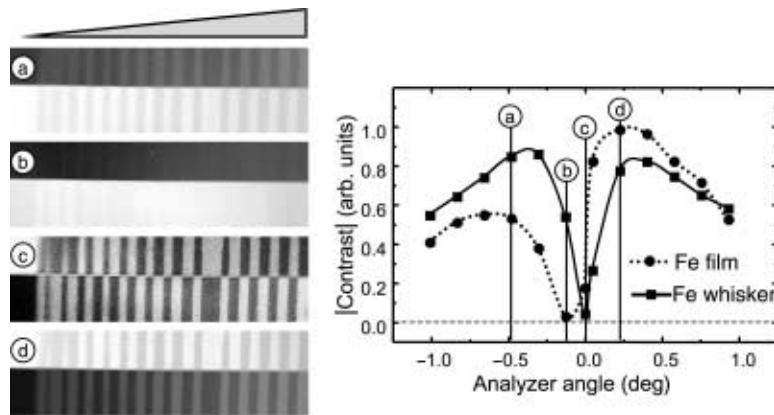


Figure 6.12. (a–d) Magneto-optic images of an (Fe whisker)/(Cr wedge)/(Fe film) structure as the analyzer is rotated. Magnetic contrast from the top film is extinguished in image (b), whereas the Fe whisker contrast is extinguished in (c). The absolute value of the contrast is shown in the adjoining plot.

Unfortunately, since this method only cancels the magnetic contrast from one layer at a time, it is difficult to sort out the magnetic structure if more than two magnetic layers are present.

The small sampling depth and topographic sensitivity of the Kerr imaging mode require preparing samples that have optically flat damage free surfaces. Bulk samples can be prepared by mechanical polishing, followed by chemical polishing or annealing to remove the remaining damage. High-quality surfaces for imaging can also be generated by evaporation or electrodeposition of thin films on flat, polished substrates. Samples may also be coated by thin, nonmagnetic films, without significantly affecting the magneto-optic images. In fact, appropriate antireflective coatings can be applied to samples in order to increase the magneto-optical contrast.<sup>43</sup>

There are also several new developments in magneto-optical imaging that are worth noting because of their potential future impact. First, near-field optical techniques are being used to overcome the resolution limits of conventional diffraction limited optics. By using scanned apertures or tips much closer than an optical wavelength from a surface, resolutions on the order of  $\lambda/10$  have been achieved.<sup>44,45</sup> So far, near-field techniques have worked best for transparent samples and transmitted light. Second, magneto-optic indicator films have been developed as an alternative to the Bitter pattern imaging.<sup>46</sup> In this method, a thin, free-standing garnet film is placed against a magnetic sample and the resulting domain pattern, induced by the sample's stray field, is imaged using a conventional polarized light microscope. Compared with the Bitter imaging, this relatively simple and inexpensive technique has the advantage of faster response to applied magnetic fields and no sample contamination. Finally, intense laser illumination has made imaging by using second harmonic Kerr effects possible.<sup>47</sup> The second harmonic mode can image structures such as domains in antiferromagnets that are not visible with conventional Kerr imaging.

In conclusion, magneto-optic imaging is a relatively straightforward technique that can directly image the magnetic structure of a wide range of materials. Magneto-optic imaging is fast, can be used with arbitrarily large applied magnetic fields, and can be used in air. The major drawback, especially for spintronics device applications, is its limited resolution of, at best, a few tenths of a micrometer, although near-field techniques may improve this in the future.

## 6.5. TRANSMISSION ELECTRON MICROSCOPY

Transmission electron microscopy (TEM), as realized on both the conventional transmission electron microscope (CTEM) and scanning transmission electron microscope (STEM),<sup>48</sup> are important tools for domain imaging and understanding spintronic devices. Utilizing highly sophisticated electron lens design and high-energy electrons, a CTEM or STEM can deliver spatial resolution of a few tenths of a nanometer. It is not surprising, therefore, that such instruments would be applied to high resolution domain imaging.

There are a wide variety of imaging modes<sup>48</sup> used in transmission microscopy. In general, an electron optically bright, high energy (200 keV) electron beam is passed through a thinned (<150 nm) sample and an image is formed. This image will reflect

both the physical structure, e.g., thickness variations, crystal grain boundaries, etc., and the magnetic structure, e.g., magnetization, domain wall location, etc., of the sample. Transmission methods designed to elucidate magnetic structure are generally referred to as either Lorentz techniques or holographic techniques. In the Lorentz methods, electrons in the beam are viewed as particles deflected by the Lorentz force produced by the magnetic field resulting from nearby magnetic material. The holographic methods are understood by viewing the microscope's field emitter as a highly coherent source of electron waves that exhibit interference when they take alternate paths to the same point in the imaging plane. The magnetic flux enclosed by these alternate paths affects this interference pattern and thereby permits the magnetic structure to be determined. We will first describe several variations of the Lorentz technique and then provide a description of one of the holographic methods.

There are three variations of Lorentz microscopy,<sup>49-52</sup> which are frequently referred to as Fresnel, Foucault, and differential phase contrast (DPC) microscopy. All sense the deflection of the electron beam as it travels through a magnetic field. In the Fresnel mode (sometimes referred to as the "defocused mode"), illustrated in Fig. 6.13(a), a defocused electron beam is transmitted through a thinned sample which has the domain structure shown schematically in Fig. 6.14(a). As depicted in Fig. 6.13(a), the Lorentz force,  $\mathbf{F} = e(\mathbf{v} \times \mathbf{B})$ , deflects the transmitted beam either toward or away from domain walls. The accompanying intensity curve shows the consequential reduction and increase in electron signal strength that signals the

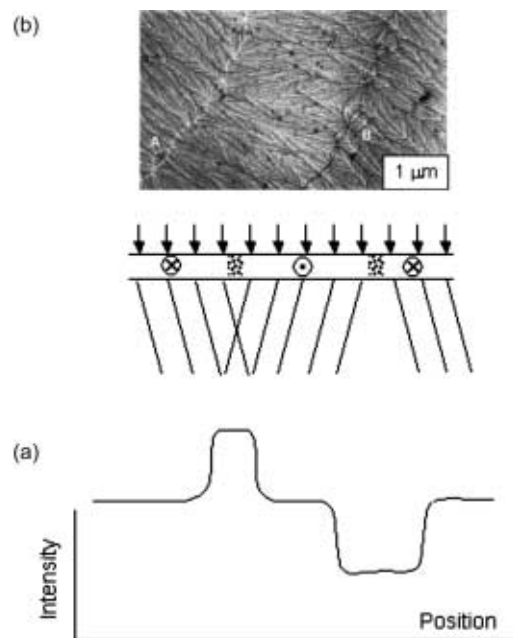


Figure 6.13. (a) Schematic depiction of deflection of defocused incident electron beam upon transmission through a thin magnetic sample illustrating the formation of bright and dark, domain wall structures. (b) Example of two domain walls, white (A) and black (B), in a thin film  $\text{Fe}_{81}\text{B}_{13.5}\text{Si}_{3.5}\text{C}_2$  sample.<sup>57</sup>

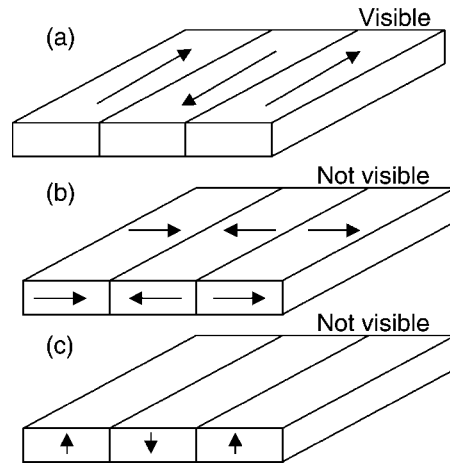


Figure 6.14. Three possible domain geometries, which will lead to observable (a) or non-observable (b,c) domain walls by using the Fresnel mode. Modified from Ref. 2.

existence of a domain wall. Figure 6.13(b) shows an image<sup>53</sup> with two domain walls, one intensified (white) and the another reduced in intensity (black).

The Fresnel mode is operationally straightforward. Domain walls are imaged with high contrast, but it is very difficult to image the internal structure of the wall itself. Also, the magnetization directions of the domains bounded by the walls must be inferred, e.g., by making use of the fact that the magnetization direction is perpendicular to the direction of “ripple” seen in the magnetization of polycrystalline samples.<sup>54</sup> The domain magnetization direction can also be determined by noting the reaction of the walls to the application of external magnetic fields. One example of the Fresnel mode applied to imaging spin valves can be found in the study of the dependence of magnetization reversal on coupling strength and direction of applied field in permalloy spin valve elements.<sup>55</sup> A second example is the study of the magnetization reversal in CoCu multilayers as a function of the number of bilayers.<sup>56</sup>

If the domain configuration to be measured is as shown in Fig. 6.14(b) or (c), the domain wall contrast mechanism is not so straightforward. In the case shown in Fig. 6.14(b), the beam deflection would be along the wall and cancellation from stray fields would occur. In the case of Fig. 6.14(c),  $\mathbf{v}$  and  $\mathbf{B}$  are parallel in the sample so no deflection would occur unless the sample was tilted to generate a magnetization component similar to Fig. 6.14(a).

The Foucault or in-focus Lorentz mode of domain imaging is illustrated in Fig. 6.15(a). In this mode, an in-focus image is formed but an edge inserted in the objective plane is maneuvered to discriminate against electrons that have been deflected to one side. This corresponds to increasing the image intensity for domains magnetized in one of the directions parallel to the edge and reducing the intensity for those domains oppositely magnetized. By moving the objective aperture, it is possible to intensify any desired magnetization direction. Figure 6.15(b) shows a Foucault image of the same region imaged by the Fresnel method in Fig. 6.13(b). The Fresnel method provides wall contrast while the Foucault method gives domain

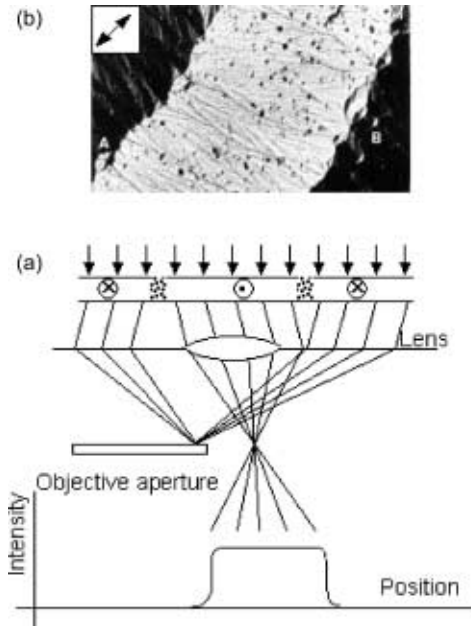


Figure 6.15. (a) Schematic of the Foucault or in-focus mode of domain imaging showing the use of an objective aperture to select out rays deflected in a particular direction to provide domain contrast. (b) An example a domain [also shown in Fig. 6.13(b)] as seen in the Foucault mode.<sup>50,53,57</sup>

contrast. When used together, these modes of TEM give a good overall description of the domain structure. However, switching between modes to image the same region with both techniques requires changes in the electron optics.

The Foucault technique has been used recently to image an active spin valve element and show the domain structure during magnetization reversal for a different spin valve structures, compositions and applied currents.<sup>58</sup> Figure 6.16(a) shows the magnetization reversal for a NiFe/Cu/Co/NiFe/MnNi spin valve structure, measuring  $10\ \mu\text{m} \times 30\ \mu\text{m}$  that has been deposited on a 40 nm alumina membrane. Currents of three different values were applied to the element to measure the GMR *in situ*. In Fig. 6.16(b) and (c), we see the domain patterns for points marked on the curves of Fig. 6.16(a) for currents of 0.3 and 3.5 mA, respectively. The difference between the domain structures for the high and low current cases is attributed to heating effects.

The DPC mode, with two exceptions,<sup>60,61</sup> makes use of a STEM. As depicted in Fig. 6.17, the focused beam is scanned across the domain structure and the Lorentz force deflects the transmitted beam. It is detected predominantly by the right or left detector elements depending on the magnetization direction in the domain. De-scan coils have been used to center the beam on the detectors in the absence of a magnetic sample. The magnetic contrast is derived from the difference in signal level at opposite detectors, which may be either half circles or quadrants. Differential phase contrast microscopy offers a more straightforward interpretation of the magnetic image than the other Lorentz methods, at the expense of requiring a more complex instrument. It shares a difficulty with the other Lorentz methods; crystallographic

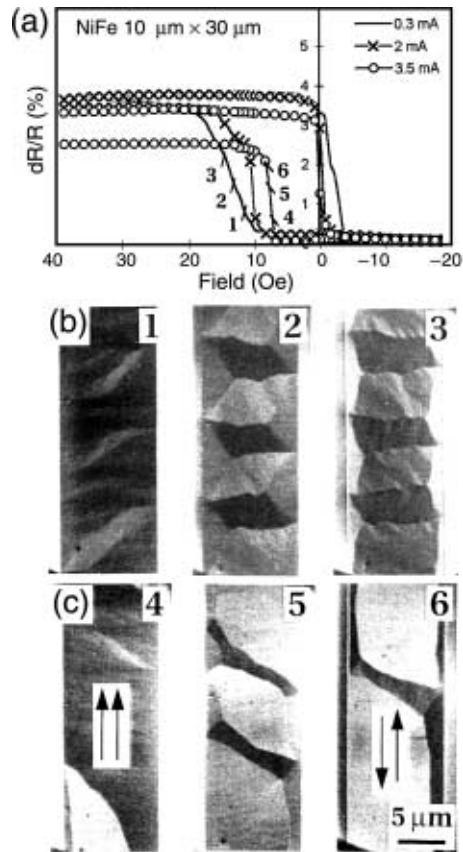


Figure 6.16. (a) GMR curves of a NiFe spin valve measured *in situ* during Foucault mode domain observations shown in (b) and (c). Three different currents were applied to the device to measure the GMR. (b), (c) Domain images of the spin valve corresponding to the measurement points indicated in (a) for applied currents of 0.3 and 3.5 mA, respectively.<sup>58,59</sup>

structure can be difficult to distinguish from magnetic structure.<sup>50</sup> Modification of the DPC detection system has proven useful in minimizing this effect.<sup>50,62</sup> Differential phase contrast has been used to study the magnetization reversal in micrometer sized, permalloy spin valve elements to see directly the effect of size on the magnetization reversal mechanism.<sup>63</sup> In a slightly earlier study using both the Fresnel and DPC methods, NiFe/Cu/NiFe/FeMn spin valve structures were imaged and studied in detail.<sup>64</sup>

Electron holography,<sup>51,66-68</sup> suggested by Gabor in 1948<sup>69</sup> as a way to reduce the effect of aberrations at high magnification, has been applied to the imaging of magnetic domains. In this technique, a field-emission electron gun is typically used to form a very bright, highly coherent source of electrons. The small source size produces the necessary lateral coherence and the relatively narrow energy distribution ensures that the electrons have a significant temporal coherence in the beam. Using such a source, it is possible to demonstrate interference between electrons that traverse paths of different length before detection, as illustrated in Fig. 6.18. Here, electrons

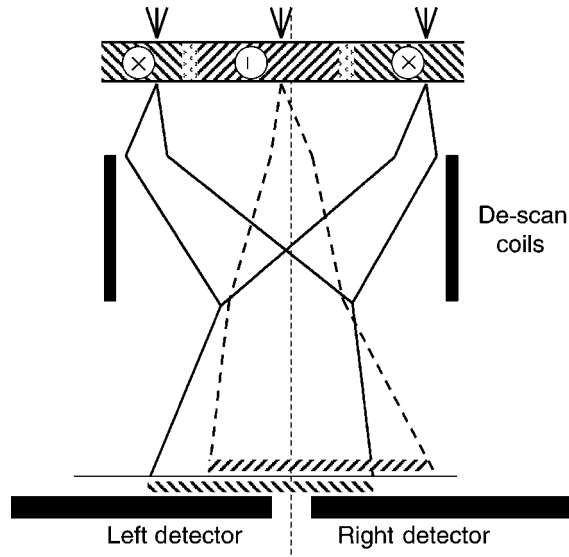


Figure 6.17. A schematic depiction of the DPC mode of imaging in which split detectors are used to monitor the angular deflections that electrons incur on transmission through ferromagnetic domains.<sup>52,65</sup>

can pass either to the right or left of a positively charged filament between two negatively charged plates; this configuration of elements is known as an “electron biprism.”<sup>70</sup> The interference fringes depicted result from the difference in phase accumulated between the two beams. The shift in phase caused by a magnetic material is visualized in Fig. 6.19 where the initial plane wavefront is distorted by the enclosed magnetic flux according to the equation,

$$\Delta\phi/\hbar = -2\pi(e/\hbar) \int \mathbf{B} \cdot d\mathbf{S} \quad (6.5.1)$$

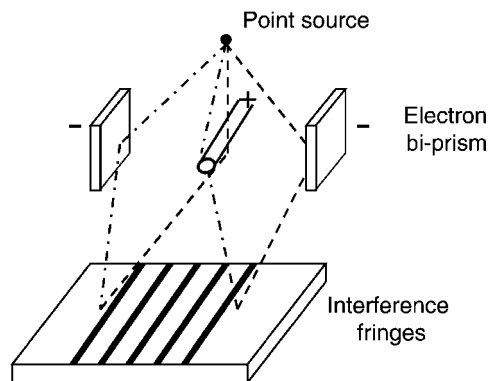


Figure 6.18. A schematic showing the interference resulting from electrons following paths of differing lengths from a high coherence source through the electron optical equivalent of a bi-prism. Modified from Ref. 66.

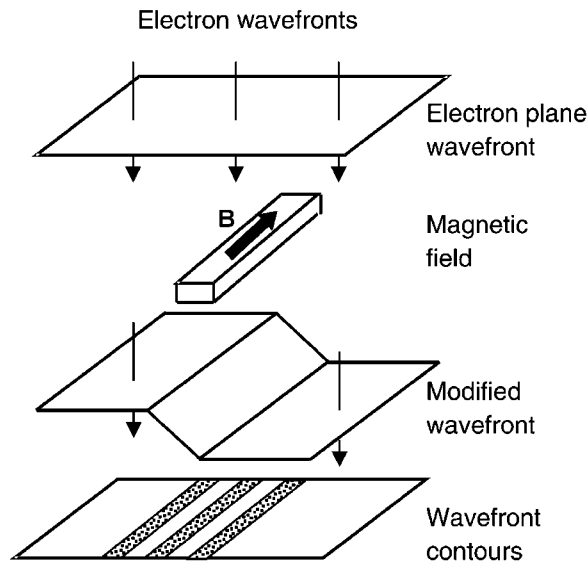


Figure 6.19. A schematic showing the evolution of a plane wave wavefront as it passes a magnetic material. Modified from Ref. 66.

Here,  $\Delta\phi$  is the difference in phase between electrons that arrive at the detector over two different paths that form a closed loop. The magnetic field,  $\mathbf{B}$ , passes through the surface  $\mathbf{S}$  enclosed by these paths; the integral gives the total magnetic flux passing through  $\mathbf{S}$ . Since the phase difference is proportional to the total enclosed flux, the wavefront contours can be interpreted directly as magnetic lines of force. An experiment that allows the measurement of the wavefront phase can therefore directly measure the enclosed flux. Indeed, the flux measurement is absolute in the sense that the surface element that corresponds to the difference between adjacent contour lines has a flux of  $h/e \approx 4.1 \times 10^{-15}$  Wb flowing through it.

The absolute mode of holographic domain imaging is shown schematically in Fig. 6.20. Here, a field emission TEM incorporating an electron bi-prism is used. The object is off center so the incident beam is both transmitted through the magnetic object and passes by it in (ideally) a field free region. The electron bi-prism causes the transmitted beam and the external (reference) beam to interfere. The resulting magnified interference pattern or hologram is composed not only of interference due to path length differences, but due to phase changes resulting from the different paths enclosing magnetic flux. The resulting hologram must be processed by optical means or, more recently, through digital processing, to display the magnetic flux pattern.

An example of a holographic image<sup>71</sup> of the magnetic flux both in and around a thin magnetic tape is shown in Fig. 6.21. The bottom 75% depicts the flux within the tape, while the top 25% of the interferogram represents the fringing field. The magnetic material consisted of a 45 nm thick cobalt film. It is important to remember that the reference beam may not always be in a field free region and the effect of stray flux may be included in images taken in this way.

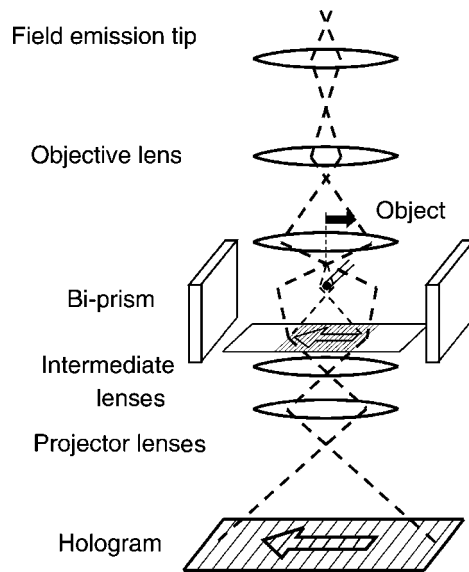


Figure 6.20. A schematic showing a setup for absolute holography. Here, a part of the wave passes through the object (right) and another part of it does not (left). A bi-prism is used to recombine the waves and produce an interferogram. Modified from Ref. 66.

In Fig. 6.22, we see another example<sup>72</sup> of absolute mode holographic imaging. Here, two 30 nm cobalt rectangles have been deposited on a 55 nm thick silicon nitride membrane. The rectangle on the left is 220 nm wide by 275 nm high, the one on the right is 300 nm wide by 275 nm high, and they are separated by 170 nm. The field is applied from right to left. The lines shown follow paths of constant magnetization. With no applied field, the magnetization lies parallel to the edges of

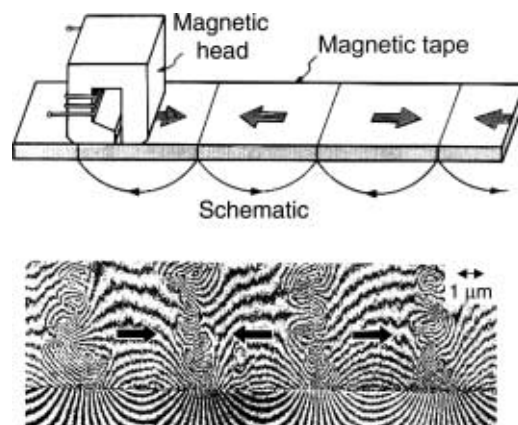


Figure 6.21. Top: Schematic depiction of recording method and recorded pattern. Bottom: Interference pattern revealing magnetic lines of force. The 45 nm thick Co film occupies the lower 3/4 of the image and the top 1/4 is free space. The magnetic lines of force are seen to lie along the magnetization direction within the Co and as a fringe field extending past the edge of the film. Modified from Ref. 67.

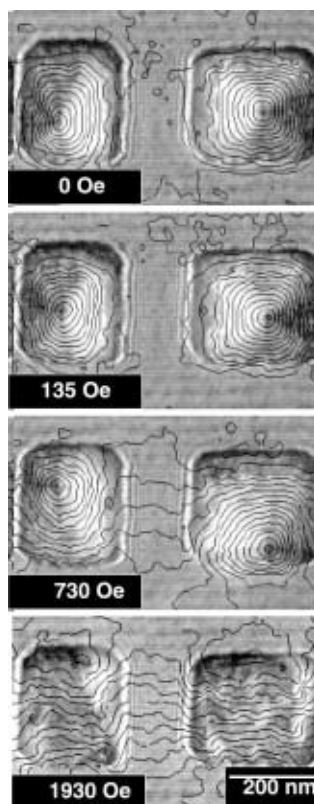


Figure 6.22. Holographic determination of magnetic lines of flux in Co rectangles of different shape for four values of an external magnetic field. Note how the two field distributions make a transition from a solenoidal configuration at zero applied field to a near-saturated configuration at 1930 Oe.<sup>72,73</sup>

the films; the lack of surface poles at the edges help to minimize the magnetostatic energy of the system. The magnetization of the two films circulates in opposite directions, as partially indicated by the shaded background in the figure. As the applied field increases the magnetic vortices of the film on the left and right move up and down, respectively, eventually disappearing as the films approach saturation at 1930 Oe of applied field.

Holographic domain imaging can also be done in what is referred to as the STEM differential mode.<sup>74</sup> Here again, an electron bi-prism is used and a hologram is recorded that reflects the phase variation due to the enclosed magnetic flux. However, in this case, there is no reference beam external to the sample. The interference is between two almost parallel beams that pass through the sample displaced by a distance of as little as 10 nm. For a uniformly magnetized sample, the enclosed flux remains constant as the beams are scanned, and the phase difference remains constant as well. This method is a particularly useful way to image small structures or domain wall profiles.<sup>74</sup>

All of the transmission methods described above have several common features. They all require thinned samples, i.e., having a thickness  $\leq 150$  nm. Sample preparation for TEM examination requires significant skill and it is important that a uniform thickness be achieved. Generally, the thinning requirement precludes being

able to examine an actual spintronic device. However, if an element of the spintronic device involves a magnetic film or films that are already thin and can be prepared on a suitable, thin substrate, then, these methods can be very useful.<sup>58</sup>

If the magnetic element must be thinned, then the thinning may have an important consequence; it may change the micromagnetics. Domain formation depends on energy minimization and as the device thickness changes the proximity of the surface becomes increasingly more important. For example, Bloch walls in the interior of a magnetic material will contain spins that are perpendicular to the surface of the material. As these walls approach the surface, the energy cost of spins oriented perpendicular to the surface gradually forces the spins to lie in the surface plane and the wall takes on the character of a Néel wall. Such a structure is known as a Néel cap.<sup>75</sup> As the sample thickness is reduced, the Néel caps present where the Bloch wall intersects each surface approach each other and eventually a vortex is formed. Transmission techniques would then respond to the average field distribution of the vortex, instead of the field distribution in the sample before preparation for observation.

As mentioned above, one great advantage of TEM methods is the high resolution available in spatial imaging. In magnetic imaging, the Fresnel, Foucault, DPC, and holographic modes have demonstrated “best” resolutions of  $\sim 10$  nm and below.

The high spatial resolution available in TEM comes about, in part, from having the sample in the magnetic field of the objective lens element. When imaging a magnetic sample, this external magnetic field can seriously perturb the magnetic state of the device under study and must be considered. Possible remedies, which may reduce the resolution, include using a special low field lens, switching off the objective lens, or moving the sample outside the lens field. A useful aspect of the field is the ability to change the component of the field in the sample plane by tilting the sample in the lens field.<sup>76</sup>

Electron holography has the advantage of being able to produce a direct display of magnetic lines of force and the absolute mode is capable of measuring, in an absolute sense, the magnetic induction. However, it has been pointed out that in domain imaging, the direction of the magnetization is generally a much more important quantity than the size of the induction.<sup>77</sup> The absolute method relies on a path for the electrons that passes outside of the sample and this can place restrictions on the fabrication and accessibility of a device under study. This has been avoided in one recent study<sup>72</sup> where the “free space” reference path was routed through the SiN substrate material adjacent to a patterned magnetic structure.

## 6.6. MAGNETIC IMAGING WITH X-RAY DICHRISM

Magnetic imaging with x-ray dichroism takes advantage of the existence of powerful new sources of synchrotron radiation. The absorption of circularly polarized x-rays in a magnetic material depends on the relative orientation of the photon helicity,  $\sigma$ , and the sample magnetization,  $\mathbf{M}$ . The difference in the absorption of light, as a function of polarization, is known as dichroism, giving rise to the name x-ray magnetic circular dichroism (XMCD) for this effect. This effect can be relatively large near atomic absorption edges. For transition metals, the spin-

orbit split  $L_3$  and  $L_2$  edges, corresponding to transitions from core 2p to valence 3d states, are usually used in XMCD measurements. Herein lies one of the main strengths of the technique; by tuning the x-rays to a particular absorption edge, elemental specificity can be achieved. The dichroism arises because the circularly polarized photons create partially polarized photoelectrons owing to the coupling between the x-ray helicity and the orbital angular momentum of the excited electron, which, in turn, is coupled to the spin of the electron by the spin-orbit interaction. The polarized electrons are excited into empty states above the Fermi level that are polarized because of the exchange interaction in the ferromagnet.

The secondary electron yield is proportional to the x-ray absorption and therefore, is sensitive to the dichroism. The dichroism, which is proportional to  $\sigma \cdot \mathbf{M}$ , will cause a spatial variation in the secondary electron intensity as the direction of magnetization  $\mathbf{M}$  changes from one domain to another. A magnetic image is obtained by imaging these secondary electrons as is done, for example, in a photoemission electron microscope (PEEM). XMCD domain imaging was first demonstrated<sup>78</sup> using an immersion lens photoelectron microscope shown in Fig. 6.23. The two stage electrostatic lens system magnifies the image of the sample and projects it on to the double microchannel plate where it is amplified before forming an image on the phosphor screen.<sup>79</sup> A digital camera and associated data acquisition electronics outside the vacuum system are not shown. Because the photons are incident on the sample at fairly grazing incidence, and it is the projection of the magnetization on the direction of photon spin that is measured, this geometry is most sensitive to magnetization in the plane of the sample. XMCD domain imaging is thus accomplished by coupling circularly polarized x-rays from a synchrotron radiation source with a PEEM system.

This domain imaging technique is nicely illustrated by the first results, which were obtained from a CoPtCr hard disk with a test pattern of alternating in-plane magnetic domains written at different recording densities.<sup>78</sup> Three XMCD images of the same 200  $\mu\text{m}$  diameter region of the disk but taken at different photon energies are shown in Fig. 6.24(a). The XMCD spectrum in Fig. 6.24(b), around the Co L edges, shows the relation between the images and the photon energies. At photon energies below the L edge, there is no magnetic contrast due to XMCD and the image at the left of Fig. 6.24(a) displays the topography of the sample surface. The middle image at the  $L_3$  resonance energy shows the domain image of the written bits. The squares are 10  $\mu\text{m} \times 10 \mu\text{m}$  and the rectangles in the row below are 10  $\mu\text{m}$  high by 2  $\mu\text{m}$  wide. The dashed (solid) line in the spectrum is for magnetization parallel (antiparallel) to the photon spin. The two different spectra can be obtained by either reversing the photon helicity or the magnetization depending on the experimental situation. Thus, at the  $L_3$  energy where the dashed line is higher in the spectrum, the bright regions in the image correspond to magnetization in the direction of the photon spin. At the  $L_2$  energy, the contrast in the image is just reversed. The image is sensitive only to one component of the magnetization; domains with  $\mathbf{M}$  perpendicular to  $\sigma$  exhibit no magnetic contrast. The XMCD effect is strong enough that domains can be seen in the raw image. Clearer images, as shown in Fig. 6.24(a), were obtained by dividing the raw image by an image taken at 810 eV photon energy in order to remove non-uniformity in the response of the optical system.

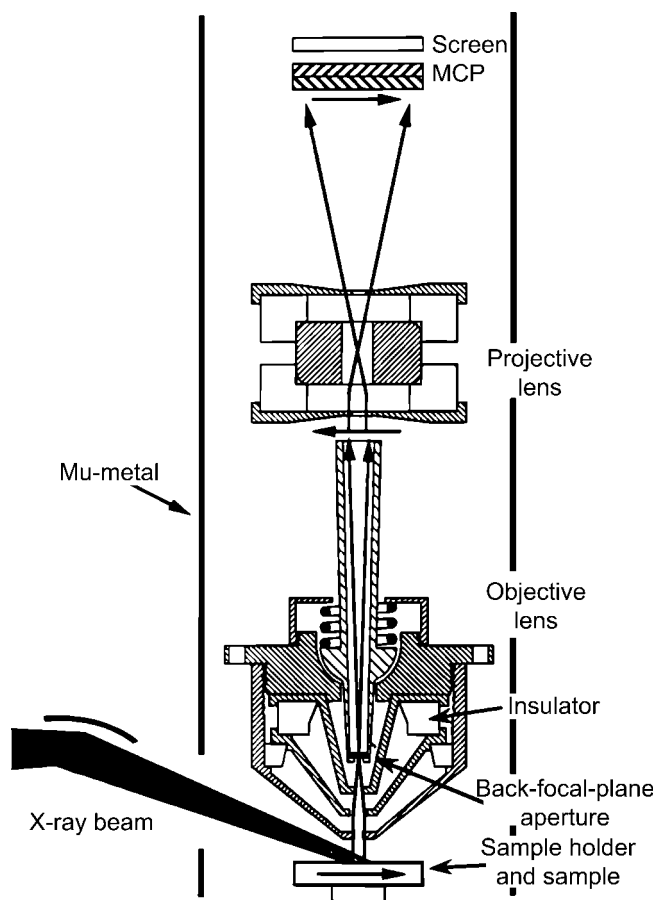


Figure 6.23. Schematic depiction of an apparatus that uses circularly polarized x-rays to produce secondary electrons that are then focused electrostatically to form a highly magnified image on a microchannel-plate (MCP) intensifier.<sup>79,80</sup>

At higher magnifications where the signal is lower, the contrast can be improved by looking at the difference between appropriately scaled images at the Co  $L_2$  and  $L_3$  energies. A row of bits  $1\ \mu\text{m}$  wide (the second row below the squares) was then clearly resolved. The resolution in this first experiment was about  $1\ \mu\text{m}$ . Improvements in the electron optics and higher x-ray fluxes from third-generation synchrotron radiation sources are predicted to lead to a  $10\ \text{nm}$  resolution.<sup>78</sup>

There are a number of strengths of XMCD domain imaging.<sup>81</sup> Its elemental specificity makes it a very powerful technique for particular problems. The magnetic measurement can also, in principle, be correlated with other core level measurements that give information on the local site, symmetry and chemical state. Because the spin and orbital moments can be determined in XMCD, the magnitude of the magnetization can be quantitatively determined. XMCD imaging has been shown sensitive enough to image 0.1 atomic layer of magnetic material.<sup>82</sup> The

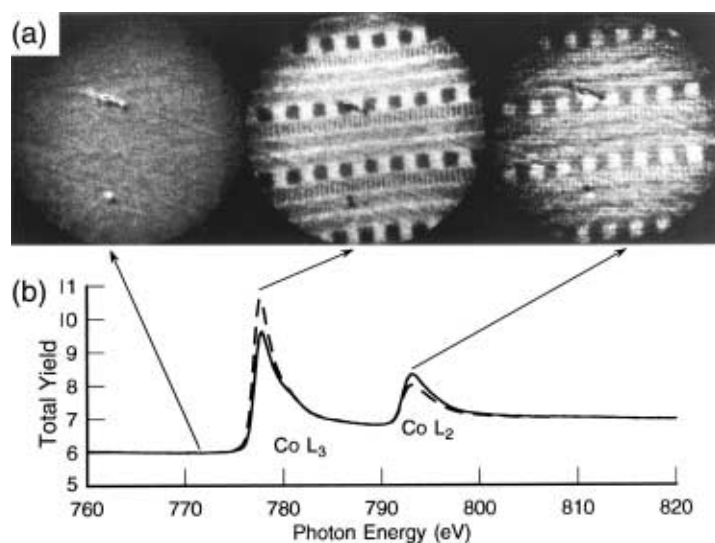


Figure 6.24. (a) Intensity image (left) and magnetic domain images (right) from a recording disk as seen by MCXD using circularly polarized x-rays of different energies. The domain rows have dimensions of  $10\ \mu\text{m} \times 10\ \mu\text{m}$ ,  $10\ \mu\text{m} \times 2\ \mu\text{m}$ ,  $10\ \mu\text{m} \times 1\ \mu\text{m}$ , and  $10\ \mu\text{m} \times 0.5\ \mu\text{m}$ , respectively. The domain magnetization lies along the direction of the rows. (b) The spectra of the L-edge dichroism and specifies the energies at which the images were taken.<sup>78,83</sup>

information depth varies with the material. It is possible to “see through” contamination or coatings. The images in Fig. 6.24 are from a disk covered with 13 nm of carbon and 4 nm of an organic fluorocarbon lubricant. The domain image depends on the relative number of secondary electrons from one domain to another, which is partially preserved in the electron cascade process that takes place as the electrons pass through overcoats. Domains can be observed through 2–4 nm of a transition metal.<sup>82</sup> This is unlike the surface sensitivity of SEMPA where the spin must be preserved and not diluted by scattering or generation of unpolarized electrons.

The XMCD can also be detected by directly measuring the helicity-dependent x-ray absorption in a transmission x-ray microscope. A condenser zone-plate images the x-ray source on the sample. A magnified image of the transmitted x-rays is formed by a second zone-plate. The spatial resolution of the first experiments on GdFe multilayer was about 60 nm.<sup>84</sup> Information is provided about the magnetic properties integrated over the path of the transmitted x-rays through the sample. The component of magnetization along the photon spin, perpendicular to the sample surface, is measured. The sample thickness should be such that the transmission is approximately 10%, which is typically of order 100 nm for transition metals. Magnetic microstructure is thickness dependent and will change on thinning a sample; this technique is particularly well suited when the sample to be measured is of the appropriate thickness. For XMCD imaging in transmission, magnetic fields can be applied, the sample need not be conducting, and the measurement is insensitive to surface contamination or moderate roughness. Scanning x-ray microscopy is a related implementation that focuses the x-ray spot on the sample and

either scans the sample or the x-ray spot while monitoring the transmitted intensity or the fluorescent x-rays from the sample.<sup>82</sup>

Linearly polarized x-rays coupled with a PEEM system to image the total electron yield have also been used to image magnetic domains.<sup>85</sup> This measurement, which is the x-ray analog of the transverse magneto-optic Kerr effect, is sensitive to the magnetization component perpendicular to the plane of incidence of the x-rays and to the electric vector of the obliquely incident p-polarized radiation. However, there is no equivalent to changing the helicity as is done in XMCD. Therefore, contrast in a domain image is obtained by taking the difference between two images measured at photon energies that have the largest difference in the total electron yield on reversal of the magnetization. The sensitivity of the domain image to  $\mathbf{M}$  perpendicular to the plane of incidence is complementary to XMCD which determines  $\mathbf{M}$  along the photon spin, and hence, in the plane of incidence. When the component perpendicular to the plane of incidence is required, or when linear polarized x-rays are most available, domain imaging using linear polarization can be useful, even though the image contrast signal is about an order of magnitude less than with circularly polarized light.

Yet, a different effect allows the imaging of domains where there is an alignment of the magnetic moments, as in an antiferromagnet, but not a net magnetization as in a ferromagnet. Near the x-ray absorption threshold, the absorption depends on whether the magnetic alignment is parallel or perpendicular to the x-ray linear polarization. This dichroism signal, sometimes referred to as x-ray magnetic linear dichroism (XMLD), is proportional to  $|\mathbf{M}|^2$  rather than  $\mathbf{M}$  as in XMCD.<sup>86</sup> Whereas XMCD requires spin-polarized d final states and spin-orbit split core levels such as the  $2p_{1/2}$  and  $2p_{3/2}$  states for an effect, XMLD additionally requires that the multiplet structure within the  $L_2$  and  $L_3$  edges can be observed. Selection rules cause a change in the spectrum depending on whether the x-ray polarization is parallel to the magnetization ( $\Delta m = 0$ ) or perpendicular to it ( $\Delta m = \pm 1$ ). XMLD was observed<sup>86</sup> in the antiferromagnet  $\text{Fe}_2\text{O}_3$ ; in that report, the imaging of antiferromagnetic domains using an x-ray microscope was also suggested. Preliminary evidence of antiferromagnetic domains was seen in images of NiO acquired by scanning the sample under the focused linearly polarized x-ray beam.<sup>87</sup> These first measurements point the way to measuring antiferromagnetic domains, but significant developments and refinements are necessary before this becomes a routine antiferromagnetic domain imaging technique. Such techniques may prove valuable in understanding the exchange biasing of a ferromagnet by an antiferromagnet, which is important for spintronics device implementation.

Finally, we mention that if instead of measuring x-ray absorption, the angular distribution of emitted electrons is measured to determine the electron wave vector  $\mathbf{k}$ , a rich variety of phenomena occur on reversing the magnetization which are loosely termed “dichroism.”<sup>88</sup> For example, using an imaging x-ray spectrometer, XMCD images obtained with angle resolved Auger electrons illustrate that a “dichroism” in the emitted electrons can be observed even when  $\sigma$  is perpendicular to  $\mathbf{M}$ .<sup>89</sup> There are also magnetic effects in photoemission angular distributions obtained with linearly polarized light.<sup>90</sup> While these chiral effects may be employed in special cases for magnetic imaging, we expect that most imaging will use dichroism in absorption and exploit the large total electron yield signal.

## 6.7. CONCLUSIONS

Some of the more relevant characteristics of the magnetic imaging methods discussed in this chapter are summarized in Table 6.1. This table serves as a useful starting point for selecting a particular imaging method, but the reader should be cautious about judging a technique based on the numbers in this table alone. For example, some important characteristics have been left out because they are difficult to quantify, such as a technique's ease of use and cost, or the difficulty in interpreting the measurements. In addition, the various parameters listed in the table are usually not independent. Optimizing one characteristic may have to be done at the expense of degrading several others. For example, an image with high spatial resolution will usually require a long acquisition time.

The row of Table 6.1 labeled resolution requires further comment. We list the best resolution demonstrated for each method as well as a value that is more typical of routine practice. However, there are several problems encountered in comparing the best resolution available for different techniques. First, it is difficult to find samples with magnetic structure known on the length scale of interest to serve as calibration samples. Second, high resolution measurements can be very demanding and consequently, are not frequently performed. Third, authors generally do not quote the resolution of their measurements. Fourth, and finally, different definitions of resolution may be used. In Table 6.1, we give our estimates of the best demonstrated resolution as obtained from the literature, and provide the references used. Several methods have the potential for improving on the quoted values.

Table 6.1. Characteristics of Magnetic Imaging Methods

	SEMPA	MFM	Magneto-optic	Fresnel, Foucault	DPC	Holography	XMCD
Contrast origin	<b>M</b>	<b>VB</b>	<b>M</b>	$\nabla \times \mathbf{B}$ , <b>B</b>	<b>B</b>	<b>B, <math>\Phi_B</math></b>	<b>M</b>
Resolution	20 [91]	40 [26]	300 [36]	$\sim 10$ [52]	$\sim 2$ [92]	$\sim 5$ [93]	300 [82]
Best [Ref]	200	100	1000	50	20	20	500
Typical (nm)							
Information depth (nm)	2	20–500	20	Sample thickness ( $\leq 150$ nm)			2–20
Acquisition time	1–100 min	5–30 min	10 ns–1 s	0.04–30 s	5–50 s	0.03–10 s	0.03 s–10 min
External Field (kA/m)	$< 1$	$< 800$	No limit	$< 500$ (vert.) $< 100$ (horiz.)		$< 100$	$< 1$
Insulators	No	Yes	Yes	No	No	No	No
Vacuum	UHV	None	None	HV	HV	HV	UHV
Topographic/crystallographic sensitivity	Low	High	High	Moderate	Moderate	Moderate	Low
Special sample requirements	Clean surface	Flat surface	Flat surface	Thin ( $\leq 150$ nm) sample + substrate			

It should be clear from Table 6.1 that no single imaging technique can solve all of the imaging problems one might encounter with spintronic devices. Rather, each technique works best for specific types of samples and each provides different magnetic information. SEMPA works well for clean ultrathin magnetic films on opaque substrates. The MFM can image the magnetic fields of buried magnetic structures. Magneto-optic techniques allow high speed imaging of magnetization dynamics in devices that are larger than a micrometer. The TEM techniques can all produce very high resolution images of patterned magnetic elements grown on transparent membrane substrates. XMCD provides element specific magnetic imaging in magnetic alloys or multilayers. In addition, the best approach to understanding some particular magnetic structure may quite often involve using several complementary techniques.

This purpose of this chapter has been to provide the reader with a limited introduction to techniques that can image the magnetic microstructure of spintronic devices. More information can be obtained by reading the larger reviews of magnetic imaging, as listed in the references, or by speaking with some of the expert practitioners of the various techniques. Ultimately, however, trying the technique is likely to be the best approach to learning which technique provides the information you need to solve your problem. You may well find that only by using several methods can you develop a complete understanding of the complex magnetic structures and interactions that can occur in nanoscale spintronic devices.

## ACKNOWLEDGEMENTS

We would like to acknowledge very helpful conversations with Michael Kelley, John Chapman, Stephen Lorentz, Michael Scheinfein and John Moreland during the preparation of this manuscript. This work was supported in part by the Office of Naval Research.

## REFERENCES

1. J. Zhu, *Magnetic Interactions and Spin Transport*.
2. A. Hubert and R. Schaefer, *Magnetic Domains* (Springer, Berlin, 1998).
3. D. J. Craik, in: *Methods of Experimental Physics*, Vol. 11, edited by R. V. Coleman (Academic Press, New York, 1974), pp. 675–743.
4. J. Unguris, D. T. Pierce, A. Galejs, and R. J. Celotta, *Phys. Rev. Lett.* **49**, 72–76 (1982).
5. K. Koike and K. Hayakawa, *Jpn. J. Appl. Phys.* **23**, L187–L188 (1984).
6. J. Unguris, G. G. Hembree, R. J. Celotta, and D. T. Pierce, *J. Microsc.* **139**, RP1–RP2 (1985).
7. D. R. Penn, S. P. Apell, and S. M. Girvin, *Phys. Rev. Lett.* **55**, 518–521 (1985); D. R. Penn, S. P. Apell, and S. M. Girvin, *Phys. Rev. B* **32**, 7753–7768 (1985).
8. E. Kisker, W. Gudat, and K. Schröder, *Solid State Commun.* **44**, 591–595 (1982).
9. H. Hopster, R. Raue, E. Kisker, G. Güntherodt, and M. Campagna, *Phys. Rev. Lett.* **50**, 70–73 (1983).
10. G. G. Hembree, J. Unguris, R. J. Celotta, and D. T. Pierce, *Scanning Microsc. Suppl.* **1**, 229–240 (1987).
11. K. Koike, H. Matsuyama, and K. Hayakawa, *Scanning Microsc. Suppl.* **1**, 241–253 (1987).
12. H. P. Oepen and J. Kirschner, *Scanning Microsc.* **5**, 1–16 (1991).
13. M. R. Scheinfein, J. Unguris, M. H. Kelley, D. T. Pierce, and R. J. Celotta, *Rev. Sci. Instrum.* **61**, 2501–2526 (1990).
14. J. A. Borchers, J. A. Dura, C. F. Majkrzak, J. Unguris, D. Tulchinsky, M. H. Kelley, S. Y. Hsu, R. Loloee, W. P. Pratt Jr and J. Bass, *Phys. Rev. Lett.* **82**, 2796–2799 (1999).

15. J. Unguris, M. R. Scheinfein, D. T. Pierce, and R. J. Celotta, *Appl. Phys. Lett.* **55**, 2553–2555 (1989).
16. J. Barnes, L. Mei, B. M. Lairson, and F. B. Dunning, *Rev. Sci. Instrum.* **70**, 246–247 (1999).
17. P. Grünberg, R. Schreiber, Y. Pang, M. B. Brodsky, and H. Sowers, *Phys. Rev. Lett.* **57**, 2442–2445 (1986).
18. S. S. P. Parkin, N. More, and K. P. Roche, *Phys. Rev. Lett.* **64**, 2304–2307 (1990).
19. J. Unguris, R. J. Celotta, and D. T. Pierce, *Phys. Rev. Lett.* **67**, 140–143 (1991); J. Unguris, R. J. Celotta, and D. T. Pierce, **69**, 1125–1128 (1992).
20. J. Unguris, R. J. Celotta, and D. T. Pierce, *Phys. Rev. Lett.* **79**, 2734–2737 (1997).
21. D. A. Tulchinsky, M. H. Kelley, J. J. McClelland, R. Gupta, and R. J. Celotta, *J. Vac. Sci. Technol. A* **16**, 1817–1819 (1998).
22. P. Grütter, H. J. Mamin, and D. Rugar, in: *Scanning Tunneling Microscopy*, Vol. II, edited by H. J. Güntherodt and R. Wiesendanger (Springer, Berlin, 1992) pp. 151–207.
23. P. Grütter, *MSA Bull.* **24**, 416–425 (1994).
24. E. D. Dahlberg and J.-G. Zhu, *Phys. Today* **48**, 34–40 (1995).
25. D. Sarid, *Scanning Force Microscopy* (Oxford University Press, Oxford, 1991).
26. L. Abelman, S. Porthun, M. Haast, C. Lodder, A. Moser, M. E. Best, P. J. A. van Schendel, B. Steifel, H. J. Hug, G. P. Heydon, A. Farley, S. R. Hoon, T. Pfaaffelhuber, R. Proksch, and K. Babcock, *J. Magn. Magn. Mater.* **190**, 135–147 (1998).
27. P.M. Kelley, private communication.
28. P. Rice, S. E. Russek, and B. Hines, *IEEE Trans. Magn.* **32**, 4133–4137 (1996).
29. A. Hubert and R. Schaefer, *Magnetic Domains* (Springer, Berlin, 1998). Section 2.6.1.
30. M. Kleiber, F. Kümmerlen, M. Löhndorf, A. Wadas, D. Weiss, and R. Wiesendanger, *Phys. Rev. B* **58**, 5563–5567 (1998).
31. C. Schönenberger, S. F. Alvarado, S. E. Lambert, and I. L. Sanders, *J. Appl. Phys.* **67**, 7278–7280 (1990).
32. M. R. Scheinfein, J. Unguris, D. T. Pierce, and R. J. Celotta, *J. Appl. Phys.* **67**, 5932–5937 (1990).
33. A. Hubert and R. Schaefer, *Magnetic Domains* (Springer, Berlin, 1998). Section 2.3.
34. S. D. Bader and J. L. Erskine, Magneto-optical effects in ultrathin magnetic structures, in: *Ultrathin Magnetic Structures II*, edited by B. Heinrich and J. A. C. Bland, (Springer, Berlin, 1994), p. 297.
35. B. E. Argyle, in: *Proc. Electr. Chem. Soc. Symposium on Magnetic Materials and Devices*, edited by L. T. Romankiw and D. A. Herman, Vol. 90–98, 85 (1990).
36. F. Schmidt and A. Hubert, *J. Magn. Magn. Mater.* **61**, 307–320 (1986).
37. A. Green and M. Prutton, *J. Sci. Instrum.* **39**, 244–244 (1962).
38. G. L. Ping, C. W. See, M. G. Somekh, M. B. Suddendorf, J. H. Vincent, and P. K. Footner, *Scanning* **18**, 8–12 (1996).
39. M. Du, S. S. Xue, W. Epler, and M. H. Kryder, *IEEE Trans. Magn.* **31**, 3250–3252 (1995).
40. B. Petek, P. L. Trouilloud, and B. E. Argyle, *IEEE Trans. Magn.* **26**, 1328–1330 (1990).
41. F. H. Liu, M. D. Schultz, and M. H. Kryder, *IEEE Trans. Magn.* **26**, 1340–1342 (1990).
42. R. Schafer, *J. Magn. Magn. Mater.* **148**, 226–231 (1995).
43. A. Hubert and R. Schaefer, *Magnetic Domains* (Springer, Berlin, 1998). Section 2.3.4.
44. E. Betzig, J. K. Trautman, R. Wolfe, E. M. Gyorgy, P. L. Finn, M. H. Kryder, and C. H. Chang, *Appl. Phys. Lett.* **61**, 142–144 (1992).
45. T. J. Silva and S. Schultz, *Rev. Sci. Instrum.* **67**, 715–725 (1996).
46. V. I. Nikitenko, V. S. Gornakov, L. M. Dedukh, Yu. P. Kabanov, A. F. Khapikov, L. H. Bennett, P. J. Chen, R. D. McMichael, M. J. Donahue, L. J. Swartzendruber, A. J. Shapiro, H. J. Brown, and W. F. Egelhoff, *IEEE Trans. Magn.* **32**, 4639–4641 (1996).
47. V. Kirilyuk, A. Kirilyuk, and Th. Rasing, *J. Appl. Phys.* **81**, 5014–5014 (1997).
48. L. Reimer, Transmission electron microscopy: physics of image formation and microanalysis, *Springer Series in Optical Sciences*, vol. 36 (Springer, New York, 1997).
49. A. Hubert and R. Schaefer, *Magnetic Domains* (Springer, Berlin, 1998). Section 2.4.
50. I. R. McFadyen and J. N. Chapman, *EMSA Bull.* **22**, 64–75 (1992).
51. M. Mankos, M. R. Scheinfein, and J. M. Cowley, *Adv. Imaging Electron Phys.* **98**, 323–426 (1996).
52. J. N. Chapman, *J. Phys. D* **17**, 623–623 (1984).
53. L. J. Heyderman, J. N. Chapman, M. R. J. Gibbs, and C. Shearwood, *J. Magn. Magn. Mater.* **148**, 433–445 (1997).
54. A. Hubert and R. Schaefer, *Magnetic Domains* (Springer, Berlin, 1998). Section 5.5.2.
55. J. P. King, J. N. Chapman, and J. C. S. Kools, *J. Magn. Magn. Mater.* **177–181**, 896–897 (1998).

56. P. R. Aitchison, J. N. Chapman, D. B. Jardine, and J. E. Evetts, *J. Appl. Phys.* **81**, 3775–3777 (1997).
57. Modified from Ref. 54, Copyright 1997, with permission of Elsevier Science.
58. X. Portier, A. K. Petford-Long, T. C. Anthony, and J. A. Burg, *J. Appl. Phys.* **83**, 6840–6842 (1998).
59. Reprinted with permission from Ref. 59, Copyright 1998, American Institute of Physics.
60. M. R. McCartney, P. Kruit, A. H. Buist, and M. R. Scheinfein, *Ultramicroscopy* **65**, 179–186 (1996).
61. A. C. Daykin and J. P. Jakubovics, *J. Appl. Phys.* **80**, 3408–3411 (1996).
62. J. N. Chapman, I. R. McFadyen, and S. McVitie, *IEEE Trans. Magn.* **26**, 1506–1511 (1990).
63. J. N. Chapman, P. R. Aitchison, K. J. Kirk, S. McVitie, J. C. S. Kools, and M. F. Gillies, *J. Appl. Phys.* **83**, 5321–5325 (1998).
64. M. F. Gillies, J. N. Chapman, and J. C. Kools, *J. Appl. Phys.* **78**, 5554–5562 (1995).
65. Modified from Ref. 53, Copyright 1984, The Institute of Physics.
66. A. Tonomura, *Electron Holography* (Springer, Berlin, 1994).
67. A. Tonomura, *Adv. Phys.* **41**, 59–103 (1992).
68. M. Mankos, J. M. Cowley, and M. Scheinfein, *Phys. Stat. Sol. (a)* **154**, 469–504 (1996).
69. D. Gabor, *Nature* **161**, 777–778 (1948).
70. G. Möllenstedt and H. Düker, *Z. Phys.* **145**, 377–397 (1956).
71. N. Osakabe, K. Yoshida, Y. Horiuchi, T. Matsuda, H. Tanabe, T. Okuwaki, J. Endo, H. Fujiwara, and A. Tonomura, *Appl. Phys. Lett.* **42**, 746–748 (1983).
72. R. E. Dunin-Borkowski, M. R. McCartney, B. Kardynal, and D. J. Smith, *J. Appl. Phys.* **84**, 374–378 (1998).
73. Reprinted, in part, with permission from Ref. 73, Copyright 1998, American Institute of Physics.
74. M. Mankos, M. R. Scheinfein, J. M. Cowley, *J. Appl. Phys.* **75**, 7418–7424 (1994).
75. M.R. Scheinfein, J. Unguris, J. L. Blue, K.J. Coakley, D. T. Pierce, R. J. Celotta, and P.J. Ryan, *Phys. Rev. B* **43**, 3395–3422 (1991).
76. S. McVitie, J. N. Chapman, L. Zhou, L. J. Heyderman, and W. A. P. Nicholson, *J. Magn. Magn. Mater.* **148**, 232–236 (1995).
77. A. Hubert and R. Schaefer, *Magnetic Domains* (Springer, Berlin, 1998). Section 2.4.4.
78. J. Stöhr, Y. Wu, B. D. Hermsmeier, M. G. Samant, G. R. Harp, S. Koranda, D. Dunham, and B. P. Tonner, *Science* **259**, 658–661 (1993).
79. B. P. Tonner, D. Dunham, J. Zhang, W. L. O'Brien, M. Samant, D. Weller, B. D. Hermsmeier, and J. Stöhr, *Nucl. Instrum. Methods A* **347**, 142–147 (1994).
80. Modified from Ref. 80, Copyright 1994, with permission of Elsevier Science.
81. J. Stöhr, H. A. Padmore, S. Anders, T. Stammer, and M. R. Scheinfein, *Surf. Rev. Lett.* **5**, 1297–1308 (1998).
82. C. M. Schneider, *J. Magn. Magn. Mater.* **175**, 160–176 (1997).
83. J. Stöhr, private communication.
84. P. Fischer, G. Schütz, G. Schmahl, P. Gutmann, and D. Raasch, *Z. Phys. B* **101**, 313–316 (1966).
85. F. U. Hillebrecht, T. Kinoshita, D. Spanke, J. Dresselhaus, C. Roth, H. B. Rose, and E. Kisker, *Phys. Rev. Lett.* **75**, 2224–2227 (1995).
86. P. Kuiper, B. G. Searle, P. Rudolf, L. H. Tjeng, and C. T. Chen, *Phys. Rev. Lett.* **70**, 1549–1552 (1993).
87. D. Spanke, V. Solinus, D. Knabben, F. U. Hillebrecht, F. Ciccacci, L. Gregoratti, and M. Marsi, *Phys. Rev. B* **58**, 5201–5204 (1998).
88. D. Venus, *Phys. Rev. B* **48**, 6144–6151 (1993); D. Venus, *Phys. Rev. B* **49**, 8821–8829 (1994).
89. C. M. Schneider, Z. Celinski, M. Neuber, C. Wilde, M. Grunze, K. Meinel, and J. Kirschner, *J. Phys.: Condens. Matter* **6**, 1177–1182 (1994).
90. C. Roth, F. U. Hillebrecht, H. B. Rose, and E. Kisker, *Phys. Rev. Lett.* **70**, 3479–3482 (1993).
91. D. A. Tulchinsky, M. H. Kelley, J. J. McClelland, R. Gupta, and R. J. Celotta, *J. Vac. Sci. Technol. A* **16**(3), 1817–1819 (1998), Fig. 6.5 (b), this paper; H. Matsuyama and K. Koike, *J. Electron Microsc.* **43**, 157–163 (1994).
92. G. R. Morrison, H. Gong, J. N. Chapman, and V. Hrnčiar, *J. Appl. Phys.* **64**, 1338–1342 (1988).
93. M. R. McCartney and Y. Zhu, *J. Appl. Phys.* **83**, 6414–6416 (1998); M. R. McCartney and Y. Zhu, *Appl. Phys. Lett.* **72**, 1380–1382 (1998).